

**POROSITY CHARACTERIZATION UTILIZING PETROGRAPHIC
IMAGE ANALYSIS: IMPLICATIONS FOR IDENTIFYING AND
RANKING RESERVOIR FLOW UNITS, HAPPY SPRABERRY
FIELD, GARZA COUNTY, TEXAS**

A Thesis

by

JOHN MORGAN LAYMAN II

Submitted to the Office of Graduate Studies of
Texas A&M University
in partial fulfillment of the requirements of the degree of

MASTER OF SCIENCE

May 2002

Major Subject: Geology

**POROSITY CHARACTERIZATION UTILIZING PETROGRAPHIC
IMAGE ANALYSIS: IMPLICATIONS FOR IDENTIFYING AND
RANKING RESERVOIR FLOW UNITS, HAPPY SPRABERRY
FIELD, GARZA COUNTY, TEXAS**

A Thesis

by

JOHN MORGAN LAYMAN II

Submitted to Texas A&M University
in partial fulfillment of the requirements
for the degree of

MASTER OF SCIENCE

Approved as to style and content by:

Wayne M. Ahr
(Chair of Committee)

Steven L. Dorobek
(Member)

Thomas A. Blasingame
(Member)

Andrew Hajash, Jr.
(Head of Department)

May 2002

Major Subject: Geology

ABSTRACT

Porosity Characterization Utilizing Petrographic Image Analysis: Implications for Identifying and Ranking Reservoir Flow Units, Happy Spraberry Field, Garza County, Texas. (May 2002)

John Morgan Layman II, B.S., James Madison University

Chair of Advisory Committee: Dr. Wayne M. Ahr

The Spraberry Formation is traditionally thought of as deep-water turbidites in the central Midland Basin. At Happy Spraberry field, Garza County, Texas, however, production is from a carbonate interval about 100 feet thick that has been correlated on seismic sections with the Leonardian aged, Lower Clear Fork Formation. The “Happy field” carbonates were deposited on the Eastern Shelf of the Midland Basin and consist of oolitic skeletal grainstones and packstones, rudstones and floatstones, *in situ Tubiphytes* bindstones, and laminated to rippled, very-fine grained siltstones and sandstones. The highest reservoir “quality” facies are in the oolitic grainstones and packstones where grain-moldic and solution-enhanced intergranular porosity dominate. Other pore types present include incomplete grain moldic, vuggy, and solution-enhanced intramatrix.

The purpose of this study was to relate pore geometry measured by digital petrographic image analysis to petrophysical characteristics, and finally, to reservoir quality. Image analysis was utilized to obtain size, shape, frequency, and total

abundance of pore categories. Pore geometry and percent porosity were obtained by capturing digital images from thin sections viewed under a petrographic microscope. The images were transferred to computer storage for processing with a commercial image analysis program trademarked as Image Pro Plus[®] (Version 4.0).

A classification scheme was derived from the image processing enabling “pore facies” to be established. Pore facies were then compared to measured porosity and permeability from core analyses to determine relative “quality” of reservoir zones with different pore facies. Pore facies are defined on pore types, sizes, shapes, and abundances that occur in reproducible associations or patterns. These patterns were compared with porosity and permeability values from core analyses. Four pore facies were identified in the Happy field carbonates; they were examined for evidence of diagenetic change, depositional signatures, and fractures. Once the genetic categories were established for the four pore facies, the pore groups could be reexamined in stratigraphic context and placed in the stratigraphic section across Happy field. Finally, the combined porosity and permeability values characteristic of each pore facies were used to identify and rank good, intermediate, and poor flow units at field scale.

ACKNOWLEDGEMENTS

I would like to thank the AAPG Foundation, Mr. Michel T. Halbouty, and Texas A&M University for providing funding for this project, without which, the science and presentation of this study would not have been a success.

I wish to thank my advisor, Dr. Wayne Ahr, for access to all of the pertinent data for this project. He provided encouragement, enthusiasm, and was my guide when I entered uncharted territory during this study. Dr. Steve Dorobek provided insight into carbonate sedimentology and image analysis techniques which proved very helpful. Dr. Tom Blasingame provided an alternate vista from the petroleum-engineering standpoint and was helpful in Clear Fork Formation evaluation.

I would also like to thank my fellow graduate students who made all of this bearable, and, at times, enjoyable. Special thanks to Bo and Elizabeth Slone, Jared Haight, John Leone, and everyone else on the ground floor of Halbouty. Your support, discussions, advice, and friendship kept me sane.

Finally, I want to express thanks to Mom and Dad, Regina and Rhonda, and the rest of my family for all of their support throughout this endeavor. You have always encouraged me with love, patience, and understanding and I owe much of my success to you. Thank you.

TABLE OF CONTENTS

	Page
ABSTRACT	iii
ACKNOWLEDGEMENTS	v
TABLE OF CONTENTS	vi
LIST OF FIGURES.....	viii
LIST OF TABLES	xi
INTRODUCTION.....	1
Purpose of Study	1
Location of Study Area	2
REGIONAL GEOLOGIC SETTING	7
Structure	7
Stratigraphy	8
PREVIOUS WORK	10
Happy Spraberry Field	10
Petrographic Image Analysis (PIA)	11
Nature of This Study	12
METHODS.....	14
Lithological Study.....	14
Borehole Logs	15
Thin-Section Petrography	15
Petrographic Image Analysis (PIA)	16

	Page
RESULTS.....	23
Lithofacies.....	23
Depositional Environment.....	29
Log Analysis	30
Core Analysis	31
Thin-Section Petrography	33
Genetic Classification of Carbonate Pores.....	34
Pore Types.....	36
Petrographic Image Analysis (PIA)	41
Mercury Injection Capillary Pressure (MICP).....	52
DISCUSSION	56
Total Porosity	56
Pore Data and Pore Facies.....	66
Petrographic Image Analysis Predicting Capillary Pressure Behavior.....	71
CONCLUSIONS.....	79
REFERENCES CITED.....	81
APPENDIX A	85
APPENDIX B	100
VITA	103

LIST OF FIGURES

Figure	Page
1. Regional paleo-map of the Permian Basin, west Texas-southeastern New Mexico	4
2. Happy Spraberry field base map showing location of wells and the John F. Lott lease	5
3. Generalized stratigraphic cross-section of the Midland Basin-Eastern Shelf transition	6
4. Shelf to basin stratigraphic correlation.....	9
5. Screen capture of Image Pro Plus® image analysis software	17
6. Calibration slide image.....	18
7. Schematic of thin-section sampling	19
8. Measurement window	21
9. Auto classification window	22
10. Core photos of oolitic and skeletal grainstone	24
11. Core photo of floatstone	25
12. Core photo of rudstone	26
13. Core photo of <i>Tubiphytes</i> bindstone.....	27
14. Core photo of siltstone	28
15. Type log for Happy field, Lott 19 #4	32
16. Porosity classification system	35
17. Photomicrographs of moldic and incomplete moldic pores	36
18. Photomicrographs of solution enhanced intergranular pores	37

Figure	Page
19. Photomicrograph of solution enhanced intramatrix pores	38
20. Photomicrograph of vuggy pores	39
21. Photomicrograph of intraparticle pores.....	40
22. Photomicrograph of primary intergranular pores.....	41
23. Photomicrographs of Lott 19 #4 well, 4960.6'	43
24. Frequency histogram of Lott 19 #4 well, 4960.6'	44
25. Lott 19 #4 well, 4923.8' photomicrographs and histogram	46
26. Lott 19 #7 well, 4978.9' photomicrographs and histogram	47
27. Lott 19 #7 well, 4981.2' photomicrographs and histogram	49
28. Lott 19 #7 well, 4950.8' photomicrographs and histogram	50
29. Lott 19 #4 well, 4971.4' photomicrographs and histogram	51
30. Summary of PIA data.....	54
31. Pore throat size distribution.....	55
32. Core porosity vs. core permeability	58
33. Core porosity vs. core permeability with lithofacies.....	59
34. Core porosity vs. petrographic porosity	60
35. Petrographic porosity by standard methods vs. image analysis porosity	61
36. Core porosity vs. image analysis porosity.....	63
37. Image analysis porosity vs. wireline log porosity	64
38. Lott 19 #4 well porosity comparison.....	65
39. Legend for pore facies model stratigraphic cross-section	68

Figure	Page
40. Stratigraphic cross section incorporating pore facies model.....	70
41. Median throat diameter vs. core permeability.....	72
42. Image analysis porosity vs. median throat diameter	73
43. Image analysis porosity vs. core permeability	74
44. Median pore throat vs. median pore size.....	77
45. Photomicrograph of non-touching vugs.....	78

LIST OF TABLES

Table	Page
1. Shape interpretation table.....	20
2. Excel spreadsheet of pore data.....	42
3. Summary of data from ten additional thin sections.....	75

INTRODUCTION

Carbonate reservoirs are commonly heterogeneous; consequently, they may require special methods and techniques for description and evaluation. Reservoir characterization, in its strictest sense, is the study of the reservoir rocks, their petrophysical properties, the fluids they contain – or the manner in which they influence the movement of fluids in the subsurface. This study focuses on the description of rocks and the pore network of a carbonate reservoir interval located at Happy Spraberry field, Garza County, Texas. Porosity and permeability relationships, wireline log signature, and a limited number of capillary pressure measurements have been examined to determine how the various factors influence reservoir quality. This study utilized a color video camera attached to a petrographic scope for acquiring pore images in thin section, and Image Pro Plus[®] image analysis software to acquire and process pore data gathered in the petrographic image analysis study.

Purpose of Study

The purpose of this study is to assess the reliability and value of digital image analysis of carbonate pores as a predictor of reservoir quality and performance. In order to accomplish this task, carbonate pores were examined in thin section to establish categories based on size, shape, and abundance. The categories were then tested to

This thesis follows the style and format of the American Association of Petroleum Geologists Bulletin.

determine the extent to which they correspond with other indicators of reservoir quality such as measured porosity, permeability, and capillary pressures. Visible porosity in each of the selected thin sections was compared to measured porosity from core analyses, porosity derived from wireline logs, and porosity from “hand counts” on thin sections (without image analysis). Pore measurements made with image analysis techniques were grouped on geometry and abundance and checked for geologic origin (genetic pore classification). Pore facies were developed to identify patterns in the porosity and petrophysical characteristics in the Happy field reservoir.

A geological model was constructed based on the origin and spatial distribution of the reservoir pore types. Studies by Hammel (1996) and Roy (1998) aided in the development of a technique for determining and comparing the best, intermediate, and poorest reservoir zones, or flow units. The results of this study suggest that automated image analysis can provide rapid and reliable measurements of pore geometry and abundance that enable the construction of reservoir pore facies. The pore facies, in turn, can be mapped to identify reservoir zones and reservoir quality. The entire process can be accomplished in a fraction of the time required to examine thin sections by the conventional “by hand” method.

Location of Study Area

Happy Spraberry field is located in Section 19, Block 2, T. & N.O.R.R. Co. Survey, Garza County, Texas on the western edge of the Eastern Shelf (Figure 1). The field is in the John F. Lott lease and includes 15 wells (Figure 2), that produce from a

carbonate interval about a 100 feet thick and presently at an average depth of about 5,000 feet below present sea-level. The reservoir consists of *in situ*, shallow marine oolitic/skeletal packstones and grainstones, floatstones, rudstones, *Tubiphytes* bindstones, siltstones, and very-fine grained sandstones. Although called Happy Spraberry field, the carbonate interval is not part of the Spraberry Formation. The Spraberry trend of siliciclastic turbidite deposits is located 150 miles southwest of Happy field in the central Midland Basin. The carbonate interval at Happy field is Early Permian (lower Leonardian) in age and is interpreted to be part of the Lower Clear Fork Formation (Tranckino, pers. comm.). The Lower Clear Fork Formation is in fact, approximate time equivalent to the basinal Dean Formation (Figure 3).

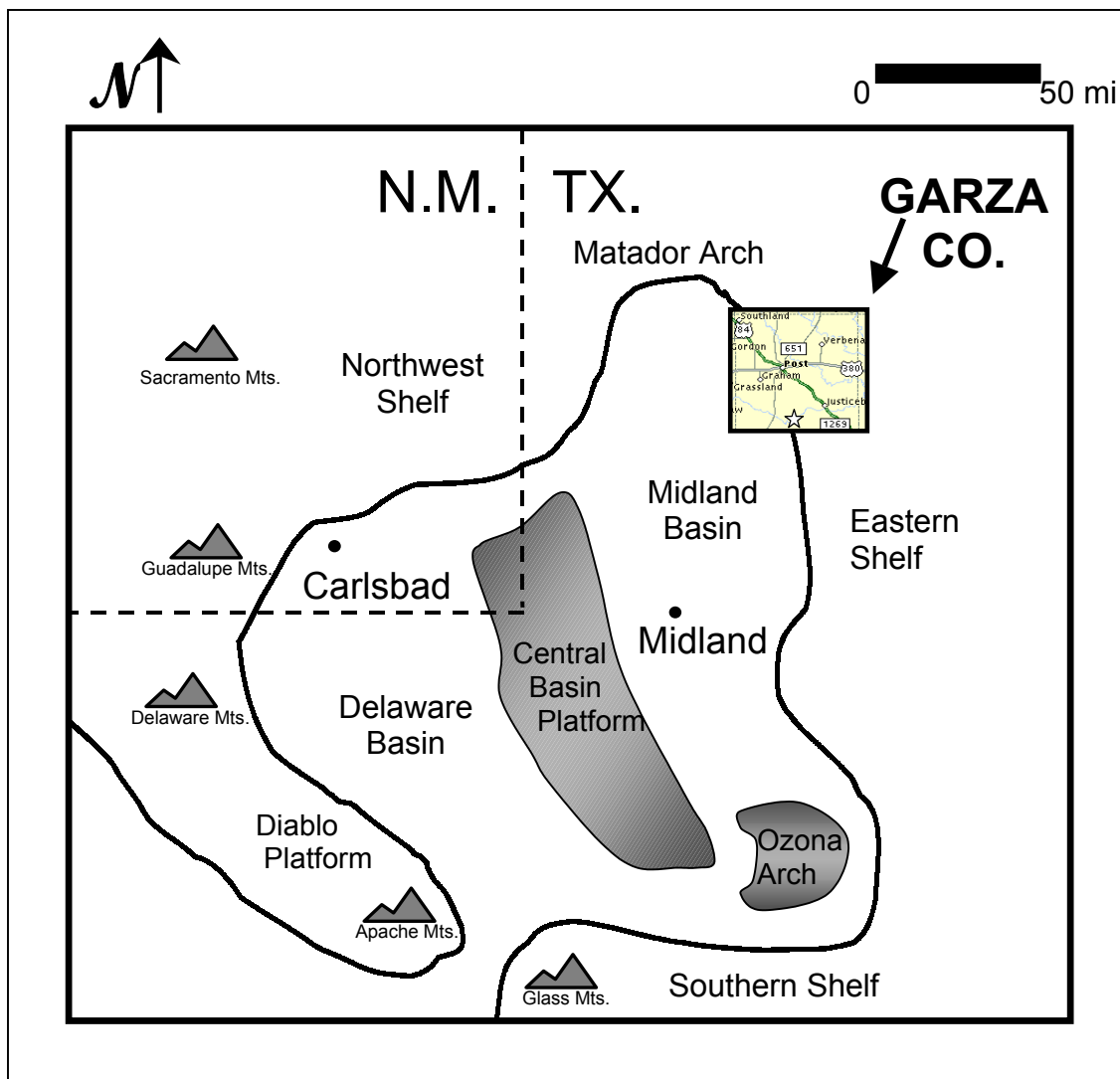


Figure 1. Regional paleo-map of the Permian Basin, west Texas-southeastern New Mexico. Note Happy Spraberry field (star) in the south-central portion of the Garza County. The approximate position of the field places it near the shelf margin. (Modified from Atchley et al., 1999).

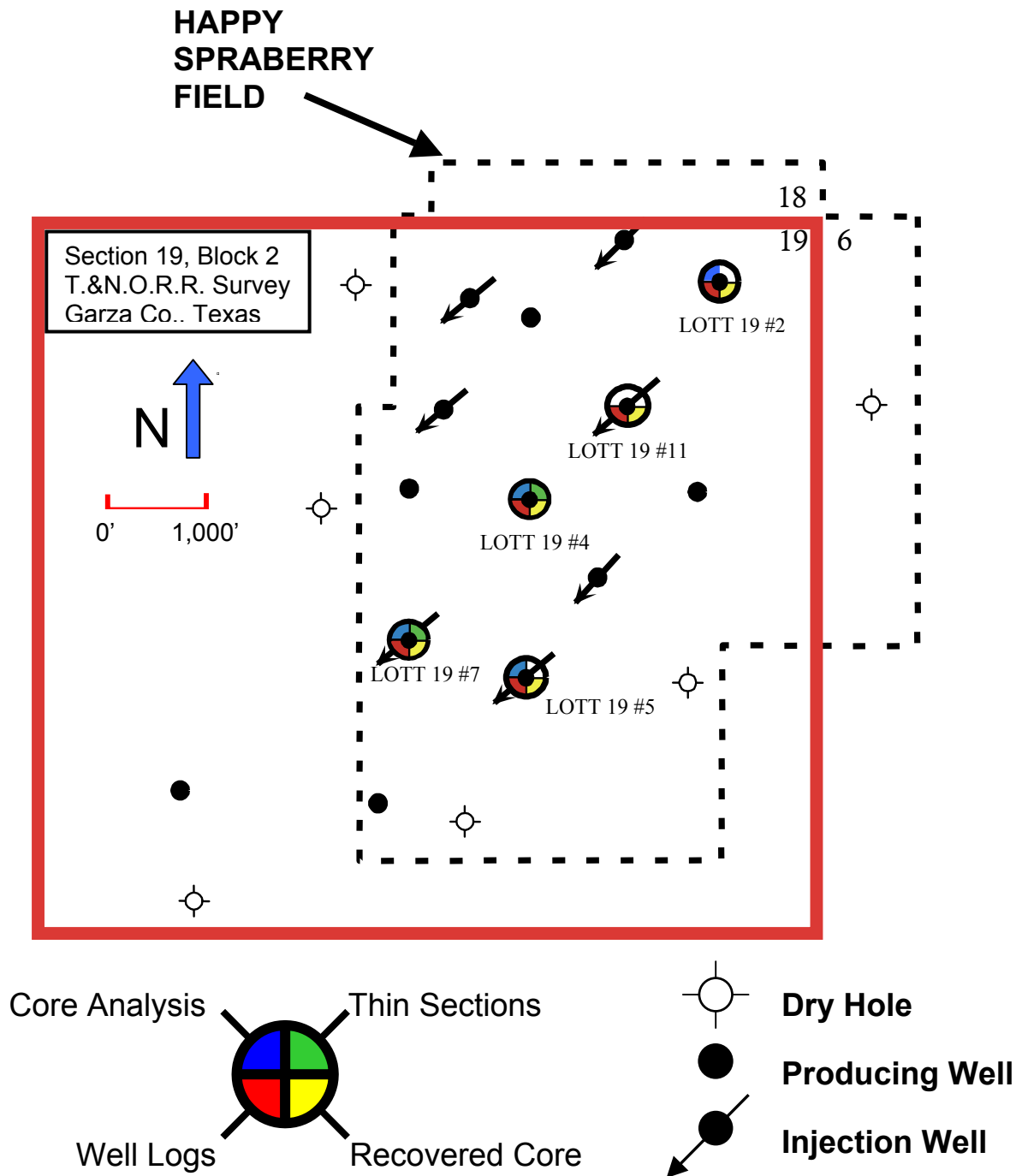


Figure 2. Happy Spraberry field base map showing location of wells and the John F.

Lott lease. Wells used in this study included Lott 19 #2, #4, #5, #7, and #11.

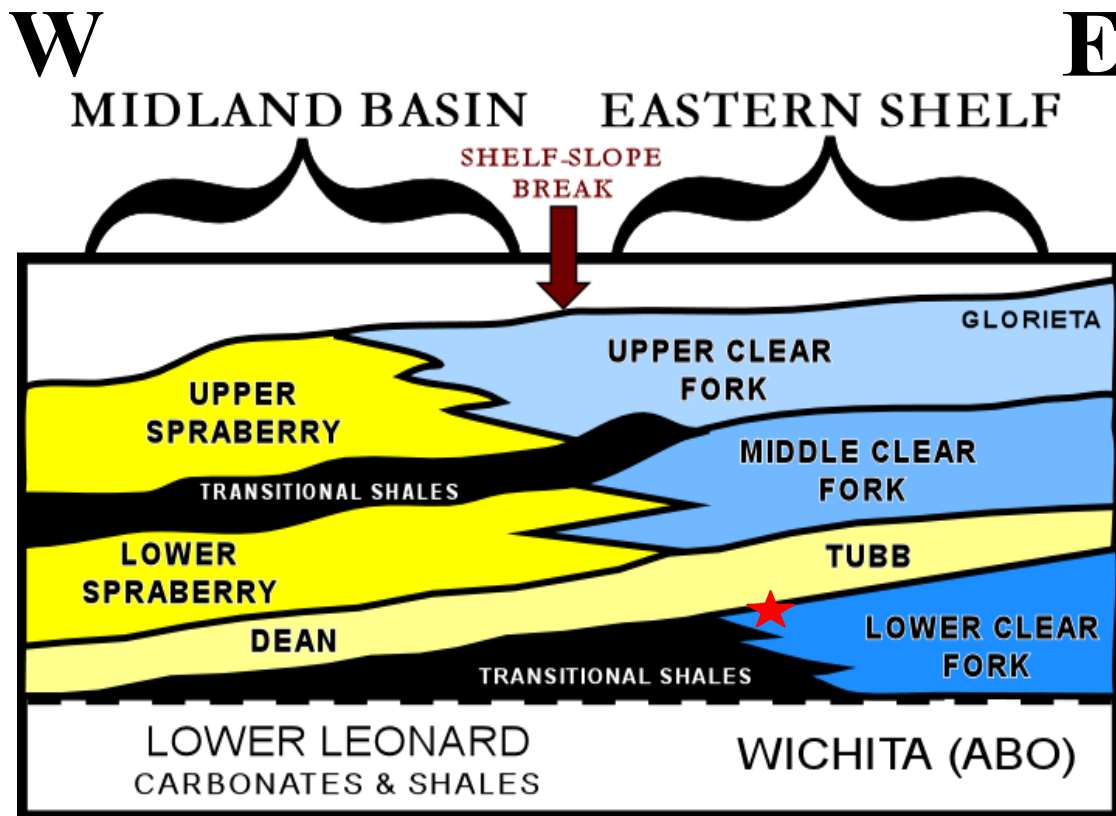


Figure 3. Generalized stratigraphic cross-section of the Midland Basin-Eastern Shelf transition. The star marks the approximate stratigraphic position of Happy Spraberry field. (Modified from Ward et al., 1986 and Handford, 1981).

REGIONAL GEOLOGIC SETTING

Structure

The Permian Basin of west Texas and southeastern New Mexico (Figure 1) is an intra-cratonic foreland basin that resulted from the impingement of the Ouchita-Marathon Fold and Thrust belt during the Gondwana-Laurassia collision. As flexure and subsidence progressed, the basin was segmented into a number of sub-basins and topographic highs (Ross, 1986). The most notable of these features is the Central Basin Platform, which separates the Delaware Basin to the west from the Midland Basin to the east. The Midland Basin is bounded to the west by the Central Basin Platform escarpment and to the east by the Chadbourne Fault Zone. This fault zone acts as the inflection point of the shelf and corresponds to the area of transition between shelf deposits and the siliciclastic deposits in the basin (Yang and Dorobek, 1994).

Happy field is located on the Eastern Shelf of the Midland Basin. During Early Permian time, the Midland Basin was a vast marine embayment. Mixed siliciclastic and carbonate deposition dominated the shelf, while siliciclastic turbidites were being shed down into the basin depocenter (Ward et al., 1986). Paleogeography places Happy field in the vicinity of the shelf-slope break. Platform geometry of the Eastern Shelf area is that of a distally-steepened ramp. Deposition of the Happy field carbonate interval took place landward of the steepening on the platform. Core descriptions suggest that deposition occurred in the distal inner-ramp environment.

Stratigraphy

The producing interval at Happy field is Early Permian (lower Leonardian) in age. Stratigraphic correlation of Eastern Shelf deposits to Midland Basin strata is often difficult because 2000 feet of vertical, structural relief separates the areas and facies changes are both common and complicated (Handford, 1981). Because of the lack of biostratigraphic control, however, the precise age of the interval is not known.

During the Early Permian (lower Leonardian), carbonate platform development was established along the western edge of the Eastern Shelf. Intervals of mixed siliciclastic and carbonate deposition were common on the shelf during this time period (Ward et al., 1986). First stages of Lower Clear Fork deposition are marked by oolitic sand bodies and isolated biohermal buildups (Montgomery and Dixon, 1998). As laterally continuous sand sheets of the Tubb Formation were being deposited, downdip deposition of the time-equivalent Dean was also starting (Mazzullo, 1991). It was concluded that the Lower Clear Fork Formation and the Tubb are both shelf equivalent to the Dean Formation (Jeary, 1978; Montgomery and Dixon, 1998; Handford, 1981)

Progradation of the platform margin during upper Leonardian is evident. Middle Clear Fork carbonates were well established as the submarine system of the Lower Spraberry fans and turbidites began the influx of siliciclastics into the basin. As progradation continued, Upper Clear Fork shelf carbonates and basinal Upper Spraberry sands were the final deposits during upper Leonardian (Figure 4). Mazzullo and Reid (1989) interpret that the Eastern Shelf portion of the platform prograded up to 24 kilometers into the Midland Basin.

The carbonate interval at Happy field is interpreted to be Early Permian (lower Leonardian) in age and part of the Lower Clear Fork Formation based primarily on seismic correlations (Barry Tranckino, pers comm). Ooid grainstones, packstones, and skeletal bindstones with segments in growth position indicate these carbonates were deposited in a shallow, tropical setting in a mid-to-distal inner ramp environment.

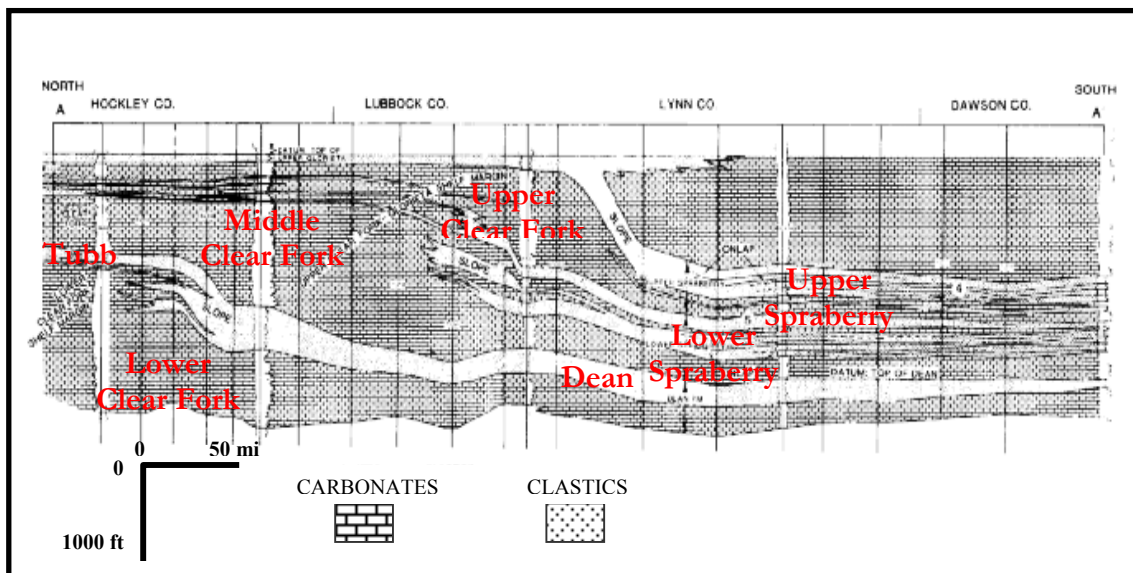


Figure 4. Shelf to basin stratigraphic correlation. Schematic cross-section showing formations and relative correlations. Note that the Lower Clear Fork and Tubb Formations are represented basinward by the Dean. See also Figure 3 for cartoon rendition. (modified from Handford, 1981).

PREVIOUS WORK

Happy Spraberry Field

Happy Spraberry field was discovered by Bennett Petroleum in 1988 on an Ellenberger Formation recompletion target in the Lott 19 #1 well. After completing a 3D seismic survey in 1989, Bennett Petroleum and Torch Energy drilled six wells in the John F. Lott Lease. Torch Operating Company acquired all production interests and drilled nine more wells by 1992. Field unitization soon followed and a waterflood program was implemented, converting several marginal-producing wells over to injection wells. Production is currently at a 40 acre spacing (Hammel, 1996).

Studies on the field have been of special interest at Texas A&M University for over 10 years because the availability of cores, core analyses, and borehole logs has provided an exquisite data set for study. Work is still underway to determine relationships between petrophysical and lithologic characteristics in order to find more reliable ways to identify reservoir quality.

Hammel (1996) conducted the initial study on the field. He created a quality classification scheme based on porosity-permeability paired values from core analyses. He then compared quality from poro-perm pairs with thin section observations to find lithologic proxies for reservoir quality. Finally, these proxies were placed in proper stratigraphic architecture to enable predictive maps of reservoir quality to be constructed.

Roy (1998) made a similar study on half of the cores in the field. His findings on reservoir quality were consistent with Hammel's (1996) and a better understanding of

the stratigraphic architecture of flow units was gained.

Mercury Injection Capillary Pressure (MICP) data from Happy field has also been studied by Ahr. MICP data yields information on pore throat size distributions within a sample. This data has also been studied to determine how pores are in communication in 3D. Waterflood programs have been implemented to enhance recovery and increase production in marginal fields. These studies have helped to provide information for improved waterflood programs.

Petrographic Image Analysis (PIA)

Digital image analysis is not new. It is simply the capturing of digital images and then analyzing image properties. This has become common practice in recent years following the appearance of high-speed desktop computers. Image acquisition and analysis software is now used by geoscientists in a wide variety of petrographic applications including textural, mineralogical, fabric, and porosity analyses.

Comparatively more work has been done on siliciclastic rocks than on carbonates. A pioneer in this effort is Robert Ehrlich at the University of South Carolina. His work helped identify pore characteristics in siliciclastic rocks by means of digital images and a software platform (Ehrlich et al., 1984; 1991a). He and others have done extensive work utilizing petrographic image analysis to relate pore and pore throat geometry to capillary pressure measurements (McCreesh et al., 1991). Work was also done on forward modeling of permeability from porosity values attained from PIA (Ehrlich, 1991b).

Image analysis on carbonates is rare compared to the volume of work done on siliciclastics. Several studies examined cathodoluminescent-zoned cements using PIA in an effort to delineate cementation events. This was helpful in determining porosity changes before and after hydrocarbon migration (Dorobek et al., 1987). Currently, a commercial laboratory in the England (Cambridge Carbonates Ltd.) performs this type of analysis as part of reservoir evaluations. PIA has also been used to identify and digitally remove generations of cementation. With this, it was possible to determine which porosity generation was responsible for the most significant pore destruction and thus to identify the “porosity killer” cement (Mowers and Budd, 1996).

Anselmetti et al., (1998) measured pore geometry in a number of modern carbonate rocks from the Bahama Banks to the Middle East. He analyzed porosity with an “order of magnitude” approach. Images of photomicrographs and scanning electron micrographs were analyzed with PIA. Pore dimensions range from less than 1 micron to a millimeter and cover three orders of magnitude. His study was of value because it focused on segmenting porosity into micro- and macroscopic components. This method established which population of pores was responsible for and contributed to overall reservoir quality. It also provided a rough parallel for this study. However, he did not discuss the implications of pore type, nor did he examine his results in a stratigraphic context.

Nature of This Study

This study differs from other image analysis studies in several ways. Most image

analysis has been performed on porosity of siliciclastic samples because purely intergranular porosity is much easier to characterize than the multiple pore types that occur in carbonates. Siliciclastic porosity is, in essence, a negative image of the adjacent quartz grains. Carbonate pores form by three end member genetic processes and are certainly more diverse than their siliciclastic counterparts. Carbonate pores may reflect multiple episodes of diagenetic alteration; therefore their origin and geometry is not always simple to interpret

A study of 52 thin sections of carbonate pores and 5 cores from Happy field was done to determine relationships between pore characteristics and reservoir quality to show that pore size, shape, and abundance are useful indicators of relative quality in reservoir flow units.

METHODS

Pore properties including area (size), aspect ratio and roundness (shape) and abundance, were measured by petrographic image analysis (PIA). Pore facies were developed from pore data and ranked from best to worst according to petrophysical attributes and pore implications on reservoir quality. Higher poro-perm pairs were associated with better quality pore facies than were lower poro-perm pairs. These differences are the basis for the quality classification system.

Lithological Study

Approximately 700 feet of slabbed core from five wells was examined under binocular microscope. Core was described in detail for depositional texture, constituent composition, porosity percent and type, pore-filling cements, and sedimentary structures (Appendix A). Rock types were classified by depositional texture following Dunham's (1962) classification system. These descriptions provided the data for identification of depositional facies and development of a depositional model for the Happy field carbonates.

Core Laboratories performed core analyses (SCAL) on cores from the John F. Lott lease wells; data include porosity, permeability, saturation, and grain density. Core porosity from the SCAL data was compared to porosity values calculated from borehole logs, from visual estimates in petrographic studies, and from petrographic image analysis. Porosity values were calculated from neutron and density logs. Values were calculated according to Asquith (1997) using neutron-density porosity cross-plot and

drilling mud corrections. Core data of porosity and permeability was graphed to determine if a linear relationship between the two values existed.

Borehole Logs

Wireline logs used in the study include gamma ray, spontaneous potential, resistivity, induction, and neutron-density logs. Gamma ray and SP logs were examined and correlated with rock type. Lithofacies were found to exhibit log signatures that were correlatable across the field.

Thin-Section Petrography

Thin sections used in studies done by Hammel (1996) and Roy (1998) were examined using standard petrographic methods. Counts of pore size and shape were made at 200 points on each thin section. In all, 52 stained samples from Lott 19 #4 and Lott 19 #7 wells were studied under plane light. Thin sections were examined to identify visible porosity, grains, cements, and matrix (lime mud or shale) (Appendix B). A micrometer ocular was used to measure pore size. Pore area was calculated from multiplying length and width pore dimensions. Pores were classified using the genetic classification scheme formulated by Ahr (Ahr and Hammel, 1999). Genetic categories were subsequently compared with size data to determine the geological relationship between pore geometry and total, visible porosity as a percentage of total thin section area. Estimates of total visible porosity were compared with total core porosity from the same depth to test for the reliability of visual, 2D estimates as predictors of volumetric,

3D porosity. High correspondence of those data indicate that visible porosity of a 2D thin section can be used as a predictor for total, 3D pore volume of a rock.

Petrographic Image Analysis (PIA)

Equipment

The image analysis system consists of a Sony DXC-290, CCD color video camera mounted on a Zeiss petrographic microscope. Images were captured by the camera and then relayed to a PC equipped with a graphics card and the commercial image analysis software program Image Pro Plus[®]. Images viewed through the microscope were focused for viewing and subsequent capture by the image analysis system (Figure 5). Magnification, light source, light intensity, and light polarity were standardized so that measurement techniques were comparable on all thin sections sampled. Images were then saved as .tif image files for later analyses.

Calibration

A calibration slide (Figure 6) was viewed under various magnifications, and the best results for a wide range of measurement sizes was found to be 12.5 diameters. This magnification was achieved with a 2.5 X objective and a 5 X phototube assembly. This magnification was solely used for this study because the “order of magnitude approach” of Anselmetti et al., (1998) would not produce specific numerical values for measurements of pore geometry. The field of view at 12.5 X magnification is large enough to accommodate entire pores of the size common to rocks in this study. Also, at

12.5X, the smallest, practical size for pore measurements was found to be about 100 square microns.

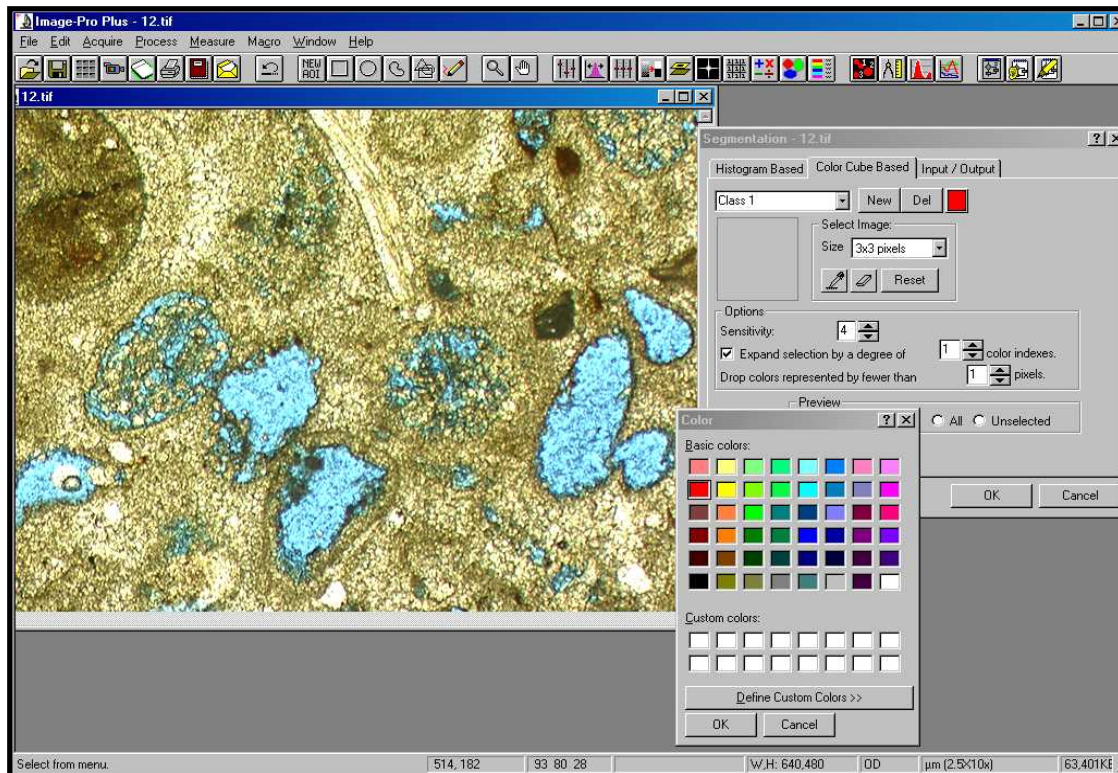


Figure 5. Screen capture of Image Pro Plus[®] image analysis software. This is a screen capture in color-segmentation mode. The cursor was placed on any pore (blue). Pixels of that blue color as well as other pixels of that color in the image (other pores) were then identified. This process was repeated until the porosity could be repeatedly identified with reproducible results.



Figure 6. Calibration slide image. This is an image in .tif format showing the calibration slide. The scale bar is 1 mm or 1000 microns in length. This image provided a specific reference length to calibrate the software for subsequent pore measurements to be taken. Image is not to scale.

Sampling

Fields of view from thin sections were chosen on the basis of ranges of visible porosity. Thin sections were studied systematically by tracking in an X-pattern (Figure 7). This method made obtaining measurements more consistent. Ten images were captured from each thin-section. The porosity value of each image was determined and average porosity was tabulated for each of the ten images. The image with the porosity value that most closely corresponded with the average porosity for the entire thin section was then analyzed in detail, as it was the most representative sample image of the thin section.

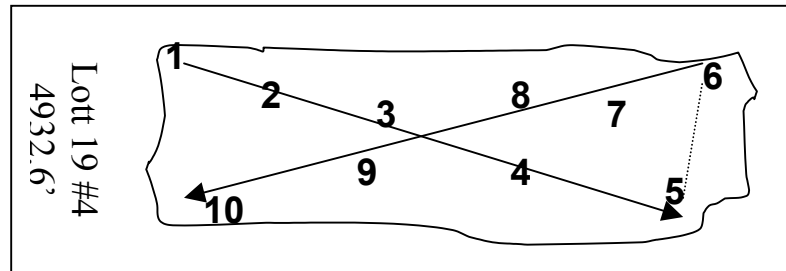


Figure 7. Schematic of thin-section sampling. 10 images per thin section were obtained using the above procedure.

Measurements





Pores were identified by a process of color segmentation (Figure 5). By placing the cursor on a pore, that pore color, and all pores of that color were electronically identified and tallied. This procedure was repeated until all pores had been accurately identified.

Measurements that would allow for quantitative analysis of carbonate pores were selected after all pores were identified. The size, shape, abundance (total), and frequency distribution of pores were logged (Figure 8). Pore area (size) was given in square microns for each pore. The total porosity seen in an image (abundance) is the ratio of the sum of all pore areas to the area of the entire image. This is also referred to as Total Optical Porosity (Ehrlich et al., 1984). Frequency is the distribution of pore sizes that comprise the total porosity.

Pore shape was determined by measuring the aspect ratio and roundness factor (Table 1). The aspect ratio measurement is equal to the ratio between the major axis and minor axis of the object; it is a measure of pore elongation (Figure 8). The roundness of an image was calculated using the formula $\text{perimeter}^2 / 4 \pi a$, where a is equal to pore area. An object with an aspect ratio of 1-1.5 is considered equidimensional.

Equidimensional shapes in this study were either circles or squares. An object was considered square if it was equidimensional and had a roundness factor above 3. An equidimensional shape with a roundness factor of less than 3 was interpreted as a circle. An object with an aspect ratio above 1.5 was considered elongate. An elongate and round shape was interpreted as an ellipse; elongate and non-round as a rectangle.

Table 1. Shape interpretation table. Combinations of aspect ratio and roundness data were used to interpret geometrical shapes to assign to pore types.

Aspect Ratio (length/width)	Roundness ($\text{perimeter}^2 / 4 \pi \text{ area}$)	Shape (geometric equivalent)
LOW (1-1.5)	ROUND (1.0-3.0)	CIRCLE 
LOW (1-1.5)	Non-ROUND (3.0+)	SQUARE 
HIGH (1.5+)	ROUND (1.0-3.0)	ELLIPSE 
HIGH (1.5+)	Non-ROUND (3.0+)	RECTANGLE 

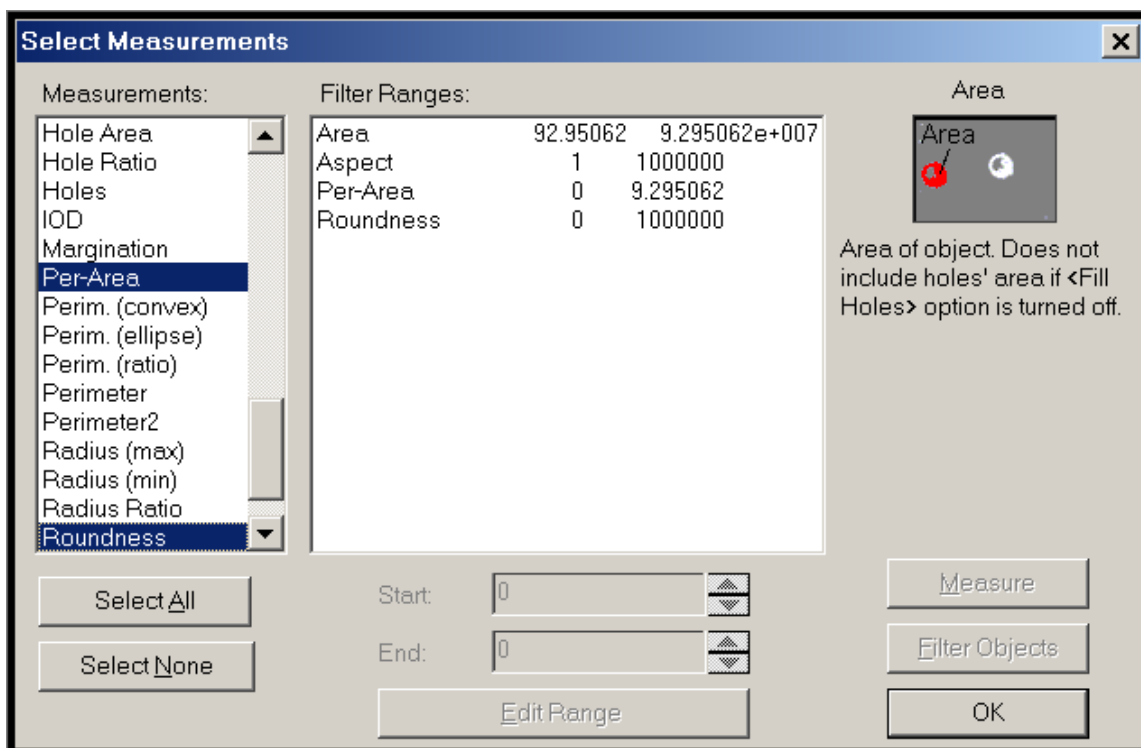


Figure 8. Measurement window. Measurements were selected according to purpose. Shown are those used in this study.

Auto-Classification

The porosity in the image was then classified into size and shape categories. The number of categories selected was determined by the number of pore types present in the sample (Figure 9). Grouped categories based on size and shape were useful in determining pore origin. This is significant because it indicates that pore geometry and pore origin may be related. Specific pore types were auto-classified such that the

average size and shape of that pore type was measured automatically. The total abundance of porosity as well as frequency distribution of pore types were also determined automatically by Image Pro Plus®.

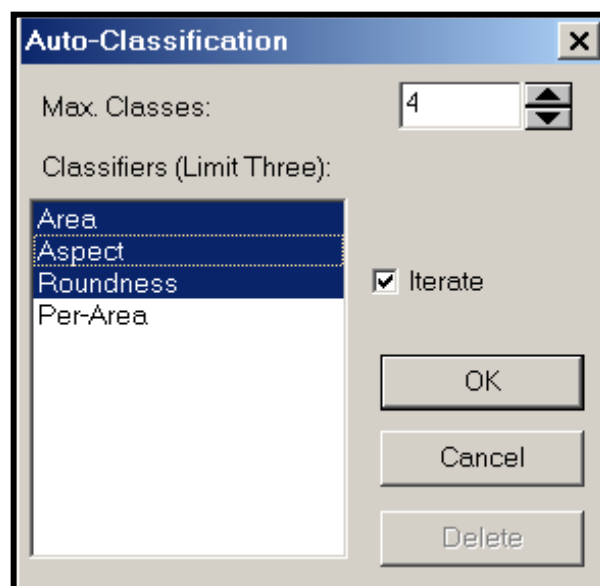


Figure 9. Auto classification window. Pores were classified according to size, aspect ratio, and roundness. In this case the pores were classified into 4 categories and then iterations were performed to determine statistics of each category.

RESULTS

Lithofacies were identified based on constituent composition, depositional texture, and sedimentary structures. Lithofacies were then correlated across the field using wireline logs and core descriptions. The field-wide distribution of lithofacies enabled a depositional model to be developed for Happy field. Lithofacies descriptions and the depositional model incorporate previous work by Hammel (1996).

Lithofacies

There are 5 lithofacies present at Happy field; oolitic skeletal grainstones and packstones, floatstones, rudstones, *in situ Tubiphytes* bindstones, and siliciclastic sediments. The principal reservoir rock is the oolitic skeletal grainstone packstone lithofacies.

Oolitic Skeletal Grainstones and Packstones

The most abundant lithofacies at Happy field consists of oolitic skeletal grainstones and packstones (Figure 10). The facies is present in all wells and ranges in thickness from 15 to 50 feet across the field. Core segments of these rocks are typically pale gray to light tan in color. Oil staining is also common and may alter the color to dark tan or brown. Ooids and skeletal allochems are commonly present only as molds after having been removed by dissolution diagenesis. Sedimentary structures are present but are obscure because there is little contrast in grain size or grain color to distinguish

them. Faint crossbedding is visible in some core intervals. This lithofacies is interpreted to have been deposited in a moderately agitated, shallow marine, tropical environment.

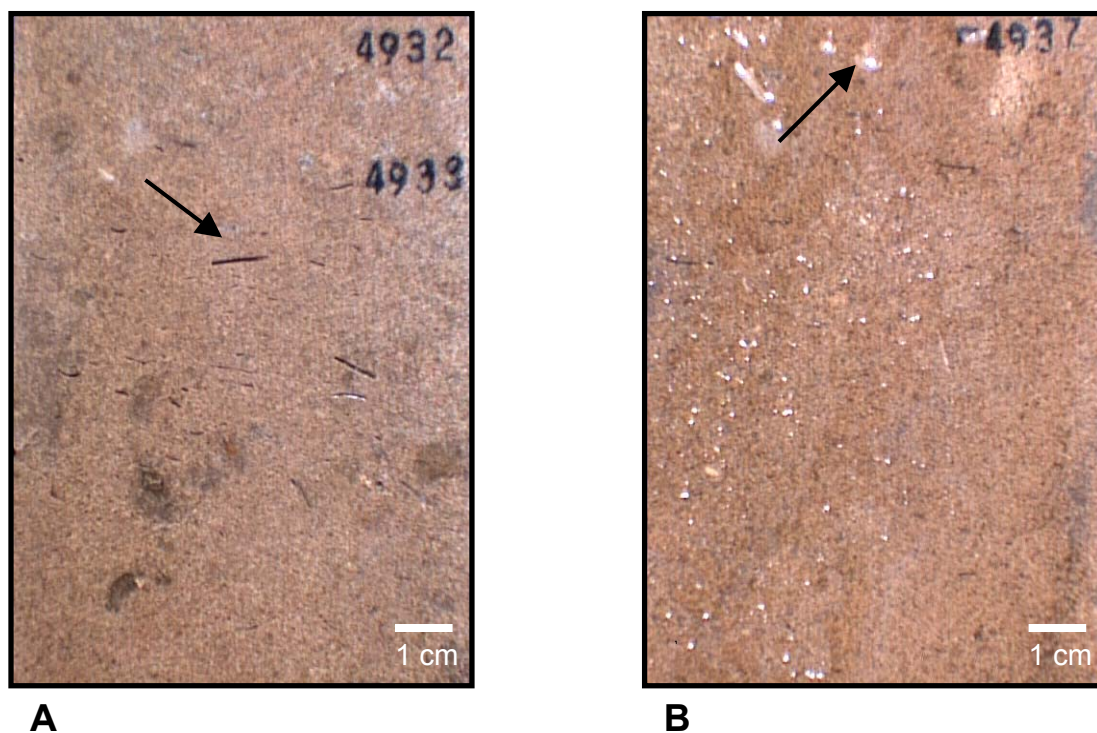


Figure 10. Core photos of oolitic and skeletal grainstone. Core samples are from 4933' and 4937', Lott 19 #4 well. A) Skeletal and oolitic grainstone. Note well-developed skel-moldic porosity (arrow) approaching 1 cm in length. B) Oil stained oolitic grainstone. Water applied for photographing (arrow) has beaded due to residual oil saturation.

Floatstones

Floatstones occur as time-equivalent deposits of the oolitic grainstone facies. Rocks are composed of a silty, lime-mud matrix with large, isolated clasts (Figure 11). The matrix is typically dark gray to black in color and may contain minor amounts (less than 10%) of marine phreatic, calcite cement. Clasts are composed of oolitic facies or skeletal fragments and may reach 5 cm in diameter. The floatstone lithofacies is interpreted to have been deposited as reworked material adjacent to the oolitic and skeletal source. The muddy matrix indicates less winnowing, probably owing to the rubble beds having been partly sheltered in the lee of the skeletal and oolitic shoals.

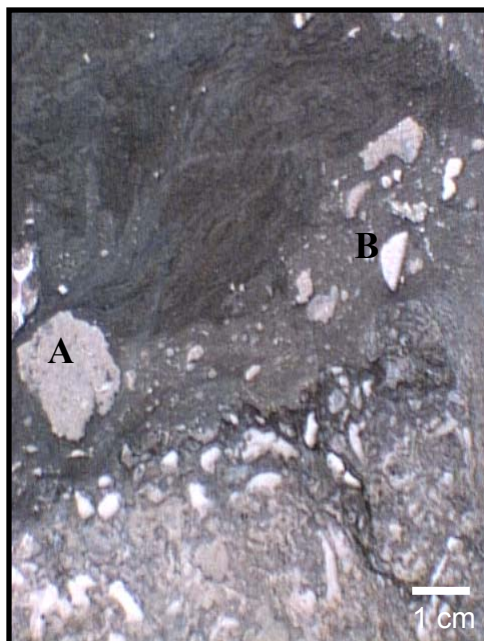


Figure 11. Core photo of floatstone. Core sample is from 4981', Lott 19 #4 well.

Isolated clasts of oolitic facies (A) and crinoid fragment (B) in a muddy matrix. Clasts exhibit crude imbricated fabric near the right portion of the photo.

Rudstones

Rudstones are interpreted to have been deposited closer to the organic buildup sources (“reefs”) because these rocks contain larger clasts and less fine matrix. Rudstones are clast-supported rocks in which clasts are typically composed of the oolitic facies or reefy, rubble material. Clasts may reach a size of 10 cm in diameter. Skeletal fragments are also commonly found whole (Figure 12) further supporting the interpretation that rudstones were deposited close to their source and underwent little transportation and abrasion. This lithofacies is interpreted to have been deposited adjacent to the oolitic grainstone facies in a low, or saddle between the two grainstone pods that was filled with rudstone debris shed off of the flanks of the buildup.



Figure 12. Core photo of rudstone. Core sample is from 4963', Lott 19 #4 well. Note brecciated, poorly sorted texture. Clasts are composed of bindstone reef rubble and are larger and more abundant than clasts in the floatstone facies.

In situ Tubiphytes Bindstone

The *Tubiphytes* bindstone facies is uncommon and was observed only in the Lott 19 #4 and #7 wells, typically laterally adjacent to floatstone and rudstone facies. It consists of clusters of organisms in growth position forming bindstones rich in bryozoans, mollusks, crinoids, and *Tubiphytes* (Figure 13). *Tubiphytes* is a type of encrusting algae that is commonly associated with *Archeolithoporella* in contributing to skeletal, biotic communities during the Permian (Sano et al., 1990). None of the bindstone facies were observed as clasts, therefore, this facies is interpreted as reef material or an *in situ*, biogenic buildup.



Figure 13. Core photo of *Tubiphytes* bindstone. Core sample is from 4971', Lott 19 #4 well. The bindstone, or reefy material is located in the right portion of the photo adjacent to floatstone clasts. Fenestellid bryozoans and mollusks are readily visible.

Siliciclastics

Siliciclastics at Happy field are composed of siltstones and very fine-grained sandstones. Rocks are light tan to light gray in color and commonly occur both above and below the entire carbonate interval. Sedimentary structures present include laminations, ripples, and soft-sediment deformation features (Figure 14). Calcite cementation is present as indicated by effervescence when dilute HCl is applied to core surfaces. Skeletal fragments are scattered in packstone stringers interbedded with the siltstones.

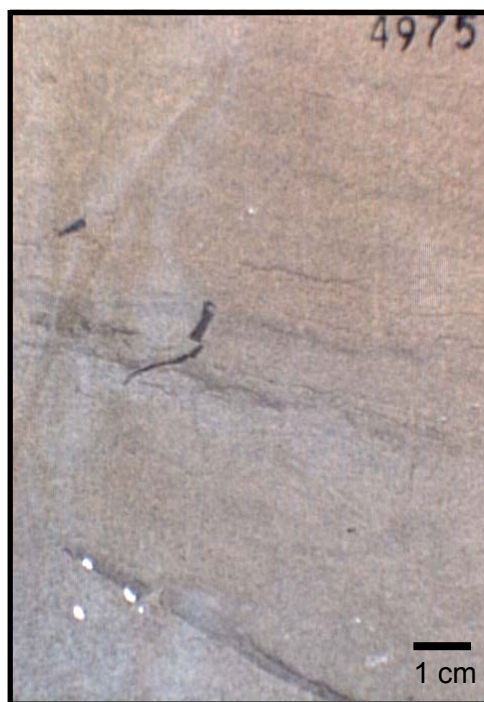


Figure 14. Core photo of siltstone. Core sample is from 4975', Lott 19 #4 well. Note wavy ripples (black) near center of photo.

Depositional Environment

A depositional model for Happy field was developed using lithologic characteristics determined from core descriptions and thin-section petrography, as well as previous work by Hammel (1996). The rocks described and facies interpreted represent deposition in a shallow marine setting. The carbonate rocks present at Happy field were deposited on a distally steepened ramp as an oolitic sand and skeletal buildup shoal complex. Siltstones and very fine-grained sandstones were deposited in an open marine setting as well, but were not the primary focus of this study.

The oolitic and skeletal grainstone and packstone facies is commonly found near the top of the carbonate section at Happy field. Ooids, skeletal fragments, and peloids are well rounded and well sorted. Average ooid grain diameter is 200-300 microns. The lack of matrix and presence of coated grains indicate deposition in shallow, agitated water. Evidence also suggests that the environment was well worked by tidal currents and was within fair-weather wave base. The sand waves represent mobile substrate similar to the oolite shoals of the St. Louis Formation (Mississippian) as described by Parham and Sutterlin (1994). Because this lithofacies is present in all cores at approximately the same depth, it is suggested that the oolitic sand wave complex is laterally continuous within the limits of Happy field.

The lithofacies of the rudstones, floatstones, and *in situ Tubiphytes* bindstones represent environments adjacent to the oolite shoals. The *in situ Tubiphytes* bindstone is a reefal facies of encrusting calcareous algae and bryozoans which form the binding framework. The rudstones and floatstones represent material shed off of the buildups.

This shedding was a result of instability as wave energy, storm activity, and normal breakdown eroded the buildups. Rudstones are interpreted to have been deposited in comparatively higher energy environments than floatstones. The rudstones contain larger intraclasts, less matrix, and were, therefore, deposited more proximal to the buildups than floatstones. The presence of coated grains and photosynthetic, binding organisms indicate shallow, tropical water that was well agitated and within fair weather wavebase and tidal currents. Sedimentary structures in the oolitic sand waves are consistent with deposition within a mobile substrate. Boundstones are evidence that biogenic buildups were able to establish themselves on the current-swept seabed. These buildups may have developed on subtle, structurally controlled, bathymetric features.

Log Analysis

Electric logs were available for the wells studied. Available were Gamma Ray (GR), Spontaneous Potential (SP), Neutron Porosity (NP), Density Porosity (DP), and Resistivity (R). GR, NP, DP, and R responses were observed to find log “signatures” that correspond to lithofacies identified in cores. It was then possible to identify and correlate lithofacies across the field with well logs where core control was absent.

GR log measures radioactivity in the borehole. Radioactive particles are relatively more abundant in clay-sized detrital material, so this is an indicator of the presence of a muddy matrix, be it siliciclastic shale or carbonate mudstone. The oolitic grainstone facies, which is close to matrix-free, has a GR response of less than 20 API units, or

what would be termed “clean”. Other carbonate lithofacies, such as rudstones and floatstones contain more carbonate mud and reflect higher GR counts.

Porosity logs may be useful in identifying porous and non-porous intervals in the various lithofacies. Log derived porosity was calculated from NP and DP logs (Figure 15) and compared to total porosity values obtained from alternate methods. Porosity in Happy field varies from 10%-26%. Generally, oolitic grainstone porosity varies between 20%-26%, rudstones and bindstones 12%-20 %, and floatstones and siliciclastics less than 12%. Though not shown, resistivity response across the carbonate interval must also be noted. R response measures how resistive rock is to electrical current and indicates whether a rock is saturated with hydrocarbons or water. The productive oolitic grainstone lithofacies is also apparent on the R response and exhibits counts in excess of 100 ohm/m, which is typical of oil-bearing zones. Non-reservoir rocks, such as floatstones and siliciclastics, register responses of less than 10 ohm/m, thus indicating they are not hydrocarbon bearing zones.

Core Analysis

Core from five wells used in the study underwent special core analysis performed by Core Laboratories. Porosity and permeability values were measured at one-foot intervals, and were graphed on semi-log plots in order to determine the relationship between the two data sets. This is useful for calculating permeability from porosity values that have been obtained by methods other than special core analysis, such as wireline porosity logs. Higher poro-perm pairs indicate higher reservoir quality.

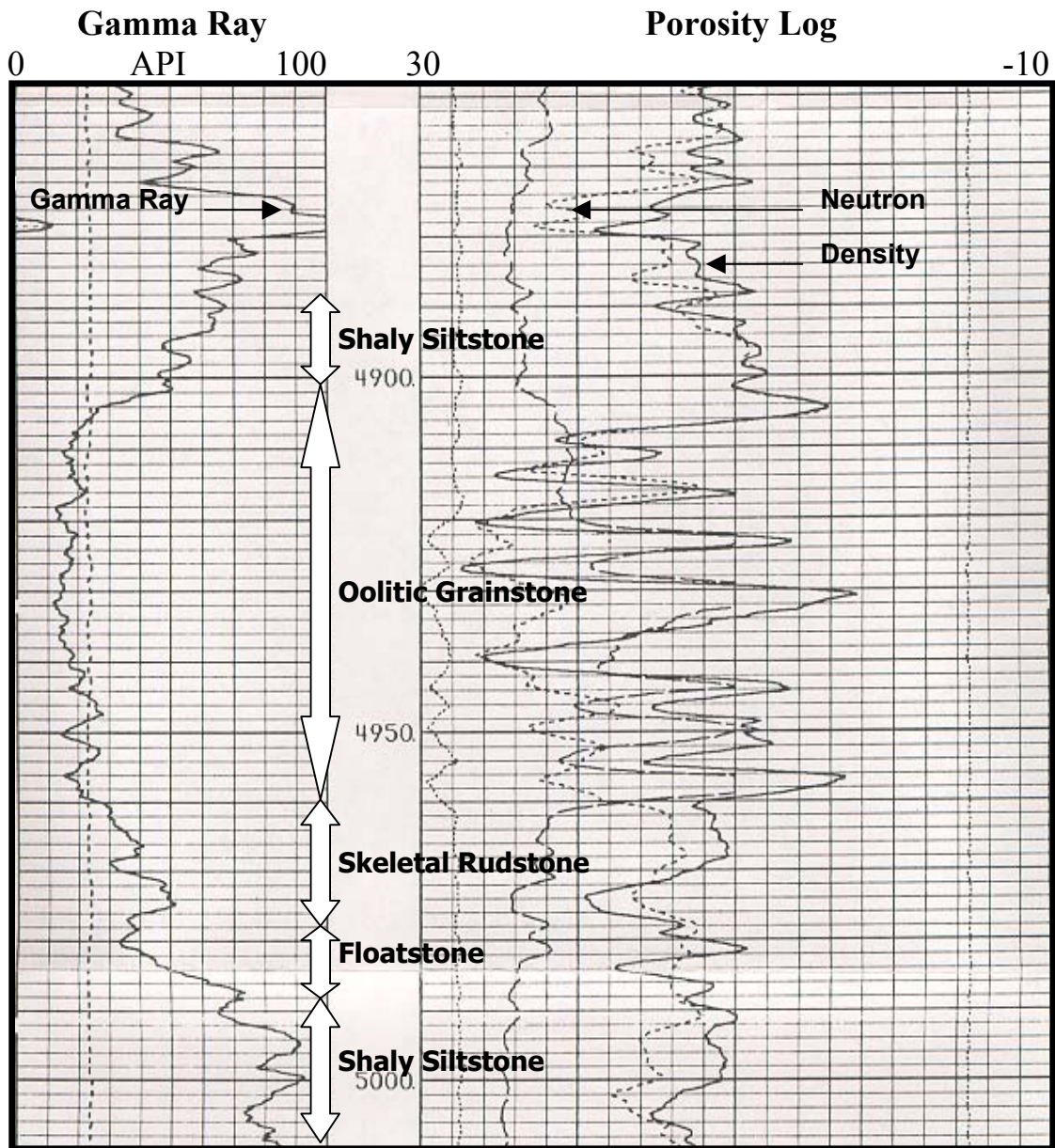


Figure 15. Type log for Happy field, Lott 19 #4. Note the “clean” GR response and the serrate NP and DP log responses to the oolitic grainstone interval. The grainstone interval was easily correlated across the field.

Thin-Section Petrography

Thin sections were examined to measure pore size, shape, frequency, and abundance. Repeat measurements were made using Image Pro Plus[®] software and the camera apparatus described in the methods chapter. The repeat measurements were made to determine if image analysis techniques could reproduce measurements obtained by traditional optical petrography.

Pore Measurements

A standard 200 point-count analysis was performed on the thin section samples to determine constituent percentages and to obtain pore data. Thin sections were analyzed and each count was tallied as porosity, grain, cement, quartz, or matrix. The percent of each constituent was then determined (Appendix B). Total porosity from petrography was compared with total porosity obtained from core analyses, log-derived porosity, and PIA porosity. This was necessary to establish that measured values of porosity from standard petrography were in agreement with values of porosity obtained by other methods. Major and minor axis dimensions were measured on counted pores to provide an estimate of pore size. Pore size was represented as pore area. Pore shape was estimated by eye as circle, square, ellipse, or rectangle. Finally, the pores were classified using the genetic system developed by Ahr and students. This genetic classification system allows for pores to be placed in the context of depositional and diagenetic processes, so that various pore types can be set in a larger context of the stratigraphic architecture at the field scale.

Genetic Classification of Carbonate Pores

Several classification systems for carbonate porosity have been developed, such as those developed by Archie (1952) and Choquette and Pray (1970). The Archie (1952) classification system is based on the texture of rock matrix, visible pore structure, and typical petrophysical behavior that would be associated with the rock. The system developed by Choquette and Pray (1970) classifies pores on the basis of whether they are fabric selective or not. It includes subsidiary descriptive sections that relate to diagenetic alteration as well as additional size modifiers. The scheme developed by Lucia (1983) classifies porosity as either interparticulate or vuggy. This takes into account that interparticle porosity and vuggy porosity have vastly different petrophysical properties. Vugs were then further classified as touching or non-touching vugs.

Carbonate pores are the result of three end-member processes- diagenetic, depositional, and fracture (Ahr and Hammel, 1999). No material fractures were observed at Happy field. Unaltered depositional pores are rare, but do exist in the form of intraskeletal pores within bryozoans. The intraskeletal pores do not contribute to overall, effective porosity. Pores at Happy field are primarily the result of a diagenetic overprint on a preexisting depositional texture present in specific lithofacies; i.e. oolitic grain-moldic porosity present in an oolitic grainstone or packstone. Accordingly, such pores would exist in an intermediate position between the diagenetic and depositional end-members of the ternary diagram (Figure 16).

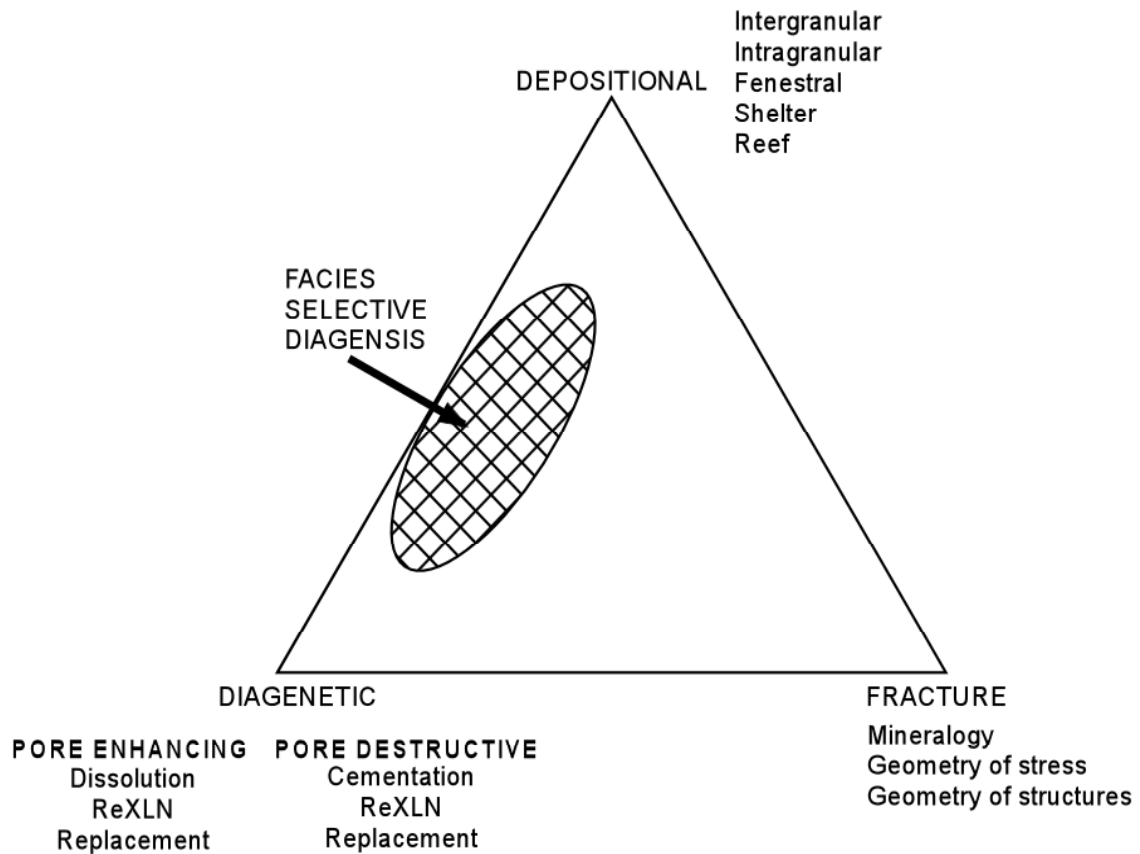


Figure 16. Porosity classification system. Pores form by three key, end-member processes. Pores at Happy field represent origin by combined diagenetic influence on the preexisting depositional template, indicated on the ternary diagram as intermediate between the two end-members. (After Ahr and Hammel, 1999)

Pore Types

Grain Moldic (M) and Incomplete Moldic (IM)

Molds and incomplete molds formed from the diagenetic dissolution of metastable grains. Molds are typically of ooids and skeletal fragments. Moldic pores exhibit sharp, distinctive outlines of leached grains, while incomplete moldic pore boundaries are less distinctive and adjacent to recrystallized remnants of the original grain. Moldic and incomplete moldic pores (Figure 17) dominate the oolitic skeletal grainstone packstone facies and are the most significant contributors to overall pore volume in the field.

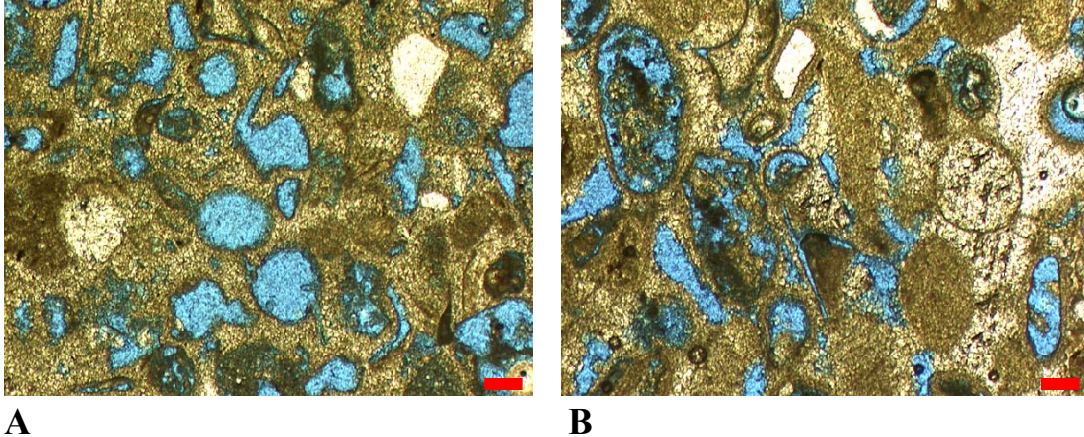


Figure 17. Photomicrographs of moldic and incomplete moldic pores. A) Sample is from Lott 19 #4 well, 4949.3'. Complete dissolution of ooid grains has resulted in well-defined pore areas. B) Sample is from Lott 19 #7 well, 4954.7'. Incomplete dissolution of ooids and skeletal grains has left grains partially intact. Scalebar = 100 microns.

Solution Enhanced Intergranular (SEIG)

Solution enhanced intergranular pores form as a result of dissolution of the cement between carbonate grains. This pore type is present in the oolitic grainstone facies and other matrix-free rocks (Figure 18). Solution enhanced intergranular pores form when primary depositional, intergranular porosity is enlarged by dissolution processes and cementation between grains is further removed.

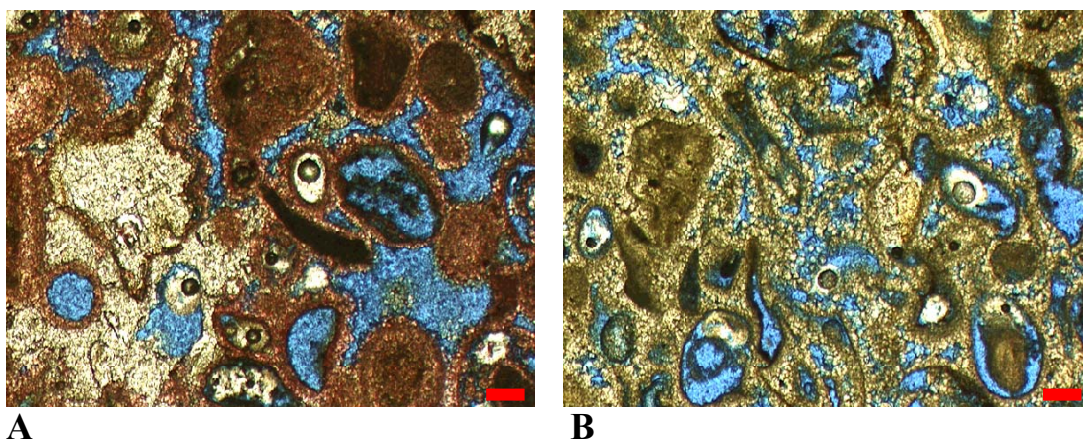


Figure 18. Photomicrographs of solution enhanced intergranular pores. A) Sample is from Lott 19 #4 well, 4930.1'. Note large, solution enhanced intergranular pores in the right portion of the photomicrograph. White area in the left portion is late burial anhydrite cement. B) Sample is from Lott 19 #4 well, 4940.8'. Solution enhanced intergranular pores are evident in this skeletal grainstone, but are not as well developed.

Solution Enhanced Intramatrix (SEIM)

Solution enhanced intramatrix porosity is present in muddier lithofacies and non-grain dominated rocks. The carbonate mud matrix undergoes stabilization to neomorphic microspar. Pores form as a result of dissolution of the peloidal, carbonate mud matrix. Where poorly developed, intra-matrix porosity occurs as fine, wispy, elongate pores. Where well developed, porosity occurs as spotty, splotchy areas of dissolution (Figure 19). This is the precursor stage to vuggy porosity. Solution enhanced intramatrix pores are the smallest in the study and contribute little to effective pore volume. Hammel (1996) identified this pore type as solution enhanced interparticle. This pore type is more aptly named as SEIM and is more consistent with its occurrence in muddier lithofacies.

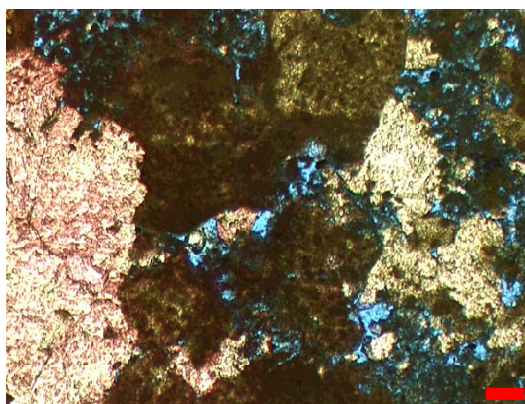


Figure 19. Photomicrograph of solution enhanced intramatrix pores. Sample is from Lott 19 #4 well, 4972.6'. The image is of well-developed intramatrix porosity adjacent to anhydrite cement (white). Wisps of faint blue/brown can be seen connecting the larger pores which are nearing vuggy in character.

Vuggy (V)

Vuggy pores occur as enlarged solution enhanced intramatrix pores (Figure 20). Pore occurrence is strictly in muddy lithofacies. Pore outlines are irregular and pore shape is typically blocky in nature. For this study, vugs are fabric selective and do not resemble preexisting component grain shapes or sizes. Vugs may contribute to overall effective porosity when interconnected by sufficient intramatrix porosity.

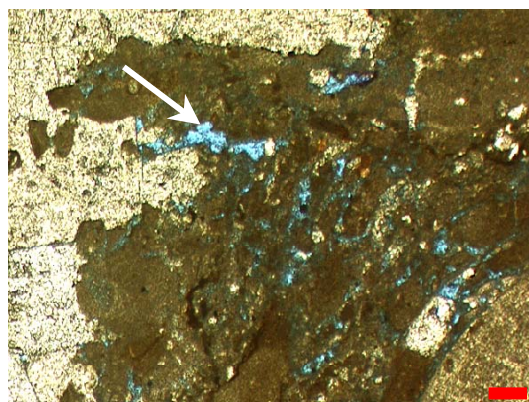


Figure 20. Photomicrograph of vuggy pores. Sample is from Lott 19 #4 well, 4980.7'. Vugs (arrow) are isolated, enlarged, solution enhanced intramatrix pores. Note large bryozoan fragment on the lower right portion of this image of a skeletal rudstone.

Intraparticle (IP)

Intraparticle porosity exists in the field in the form of intraskeletal pores. These pores are depositional in nature in that they existed before any type of diagenetic alteration took place. It is most common in bryozoan mesopores (Figure 21) and within gastropods and is insignificant in contribution to overall porosity.

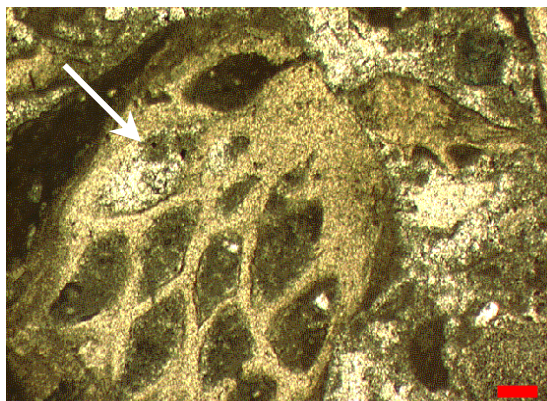


Figure 21. Photomicrograph of intraparticle pores. Sample is from Lott 19 #7 well, 4967.2'. Large bryozoan fragment with intraskeletal porosity in zooecia. Some of the porosity has been occluded by later generation, blocky, equant calcite.

Primary Intergranular (PIG)

Primary intergranular porosity exists as original void spaces between quartz grains and is present in siltstones and very fine-grained sandstones at Happy field (Figure 22). This type of porosity occurs as depositional processes winnow out clay-sized particles and pore space is preserved. This type of porosity provides minor effective porosity and was not of interest in this study.

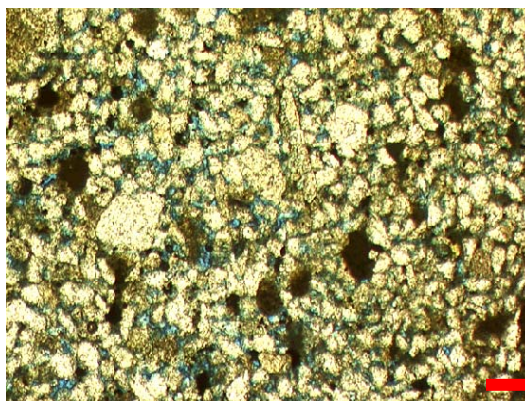


Figure 22. Photomicrograph of primary intergranular pores. Sample is from Lott 19 #7 well, 4991.6'. This siltstone retains original depositional porosity avoiding pore-destructive cementation.

Petrographic Image Analysis (PIA)

Pores were identified and measured using petrographic image analysis. Pores were classified according to geometry and the results indicate that pores that are geometrically similar share the same origin. Image analysis data yielded information on size, shape, frequency, and abundance of pores. Pore facies were then developed from cumulative frequency histograms that incorporated all image analysis data. Pore facies were ranked according to pore attributes (size, shape, and frequency) as well as petrophysical properties (total porosity, or abundance, and permeability).

Data

Pore data was exported from Image Pro Plus[®] to Excel spreadsheets (Table 2) and processed. Pertinent information on pores was processed into frequency histograms that incorporated the five data parameters; pore size, shape, type, frequency, and abundance. Table 2 is the data measurements spreadsheet for Lott 19 #4, 4960.6'.

Table 2. Excel spreadsheet of pore data. Interpretations of shape were made, the remaining data was utilized in the histograms.

Color	Class	# of Objects	% of Objects	Total Area	% Area
Red	1	74	36.633663	15460.354	3.9124074
Blue	2	119	58.910892	61519.523	15.568172
Tan	3	9	4.4554458	318182.28	80.519424

Color	Mean Area	Mean Aspect Ratio	Mean Roundness	Total Per Area	% of Per Area
Red	208.92369	2.9071846	1.369861	0.00531575	3.9124069
Blue	516.97076	1.54058217	1.4153757	0.02115234	15.568175
Tan	35353.586	1.9445627	5.888195	0.10940105	80.519417

This sample is a skeletal packstone with complete and incomplete grain moldic porosity. Molds are mainly leached skeletal fragments (Figure 23A). Porosity was identified, categorized, and processed to obtain an image that showed pores after classification (Figure 23B). Histograms of pore data (Figure 24) were made in order to test for relationships between categories of pore data. Also, porosity abundance obtained from image analysis data was compared to porosity values obtained by alternate methods, including core analyses, thin-section petrography, and log derived porosity.

Histograms

Figure 24 incorporates all pore data. Size is represented on the x-axis. Four size categories, or bins, were arbitrarily set at 100-1,000, 1,000-10,000, 10,000-50,000, and 50,000+ square microns. Pores were assigned to the appropriate size category and frequency of occurrence was plotted on the y-axis. Pore types were color coded such that dark blue=moldic, light blue=incomplete moldic, red =solution enhanced intergranular, brown=solution enhanced intramatrix, and vuggy=yellow. Porosity abundance along with permeability are also noted for each sample.

Pore shapes were interpreted from image analysis data on the basis of paired values of aspect ratio and roundness. Shapes were used to aid in the identification of pore classes. In the end, pore size, shape, origin, as well as contribution to total porosity abundance can be viewed simultaneously with ease.

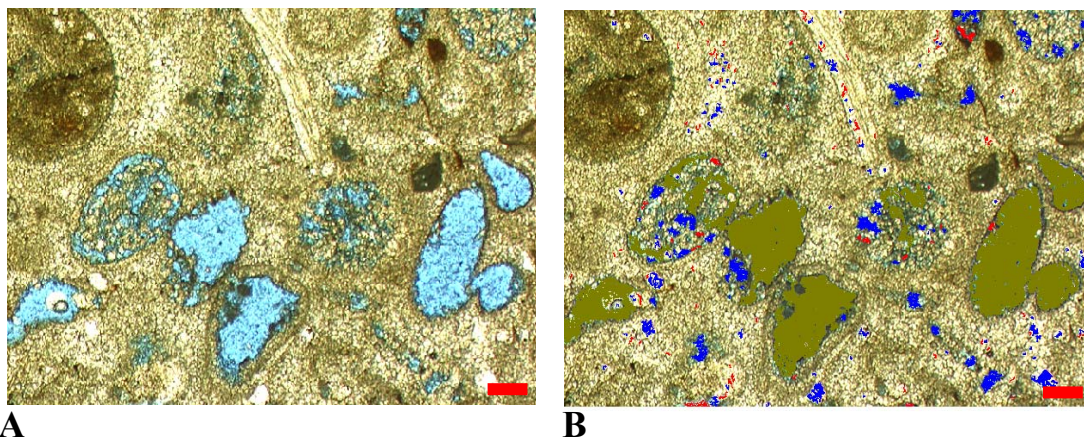


Figure 23. Photomicrographs of Lott 19 #4 well, 4960.6'. A) Image of skeletal packstone before image analysis process. B) Pores have been classified based on geometry into categories of complete molds (tan) and incomplete molds (blue and red).

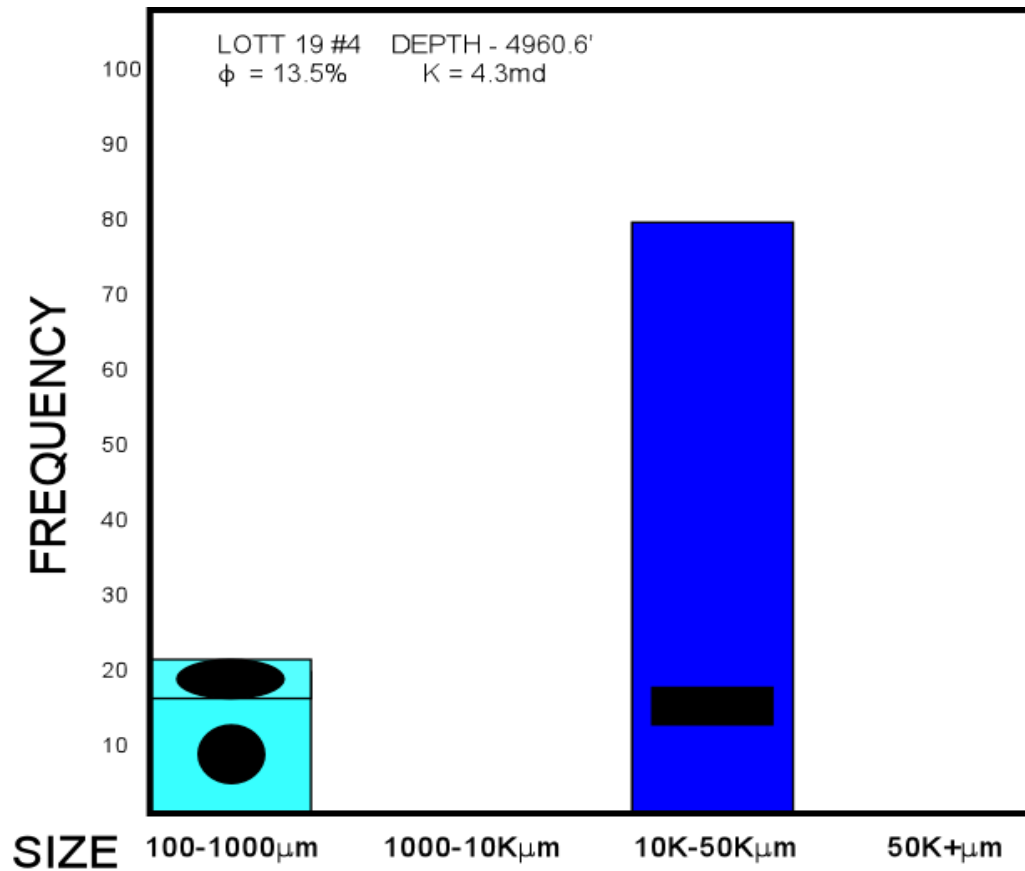


Figure 24. Frequency histogram of Lott 19 #4 well, 4960.6'. The histogram indicates that the pore network is composed of large, rectangular, moldic pores and smaller, incomplete moldic pores. The small, incomplete moldic pores do not provide adequate connectivity, as indicated by only 4.3 md of permeability.

Pore facies are both fabric and facies selective. Trends in image analysis pore data lead to the development of pore facies. A stratigraphic interval and petrographic samples within that interval would share similar features in the cumulative frequency histograms. The observations of patterns and trends in the histograms aided in the identification and ranking of four pore facies present at Happy field.

Pore Facies

Four pore facies at Happy field were identified and ranked for reservoir quality. Quality rankings are “best”, “intermediate”, and “worst”. The worst pore facies was subdivided into two distinctive, identifiable pore facies.

The highest quality or “best” pore facies occur in the oolitic skeletal grainstones at Happy field. Pore types are commonly moldic and solution enhanced intergranular pores. An example of this pore facies is Lott 19 #4 well, 4923.8’ (Figure 25). The facies has well developed, complete moldic porosity of ooids and skeletal fragments. Solution enhanced intergranular porosity is also present. These pores are present as a result of diagenetic leaching of grains and interstitial cement. The frequency histogram for the sample (Figure 25) shows that large intergranular pores are present in combination with large moldic pores. This pore facies typically has 15-25% porosity and 12-25 md of permeability. An additional, representative sample of the oolitic grainstone pore facies is present in the Lott 19 #7 well, 4978.9’, in the grainstone interval (Figure 26).

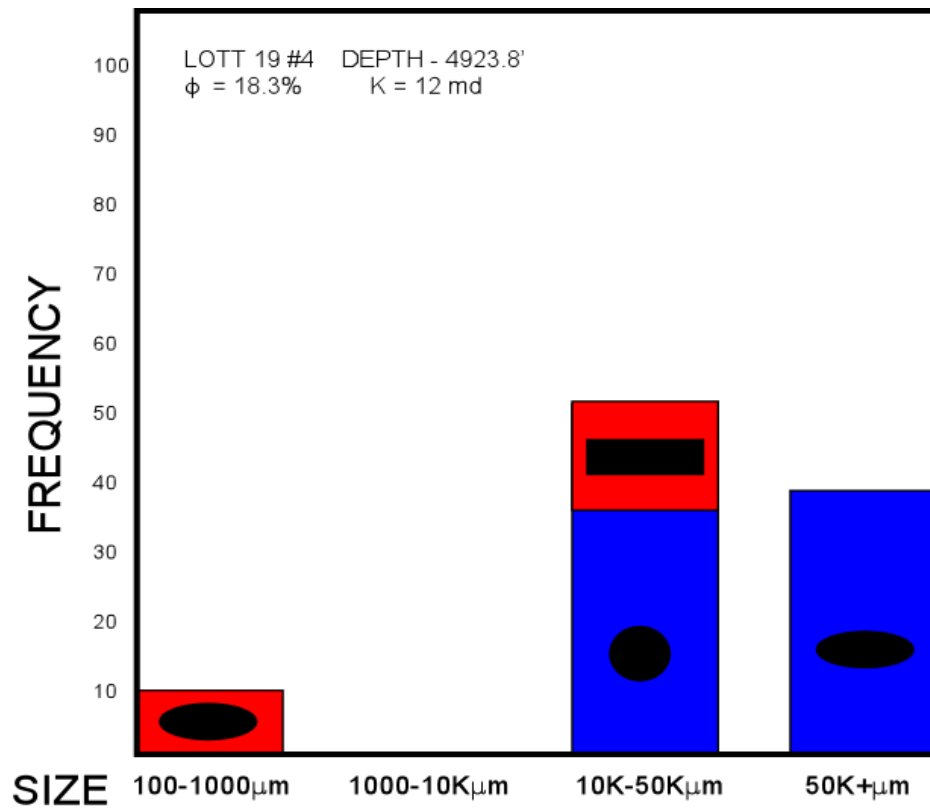
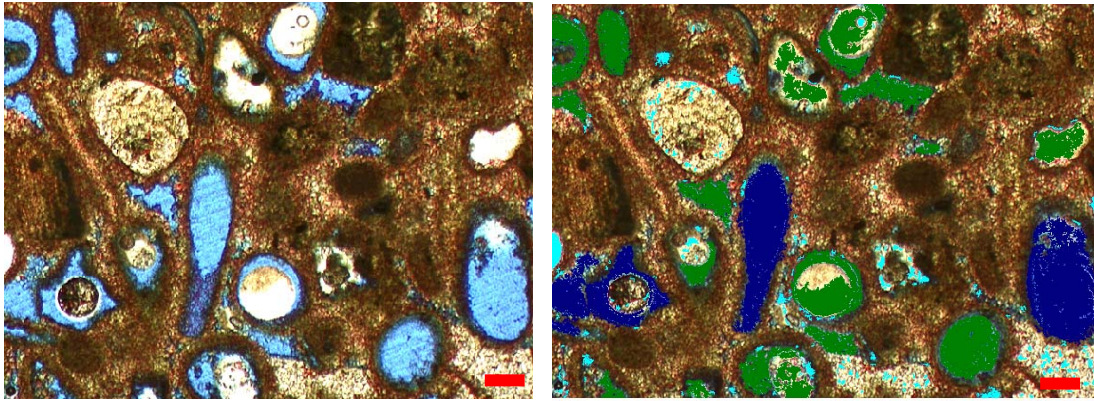


Figure 25. Lott 19 #4 well, 4923.8' photomicrographs and histogram. Note that solution enhanced intergranular pores exist on two orders of magnitude of less than 1000 and larger than 10000 square microns.

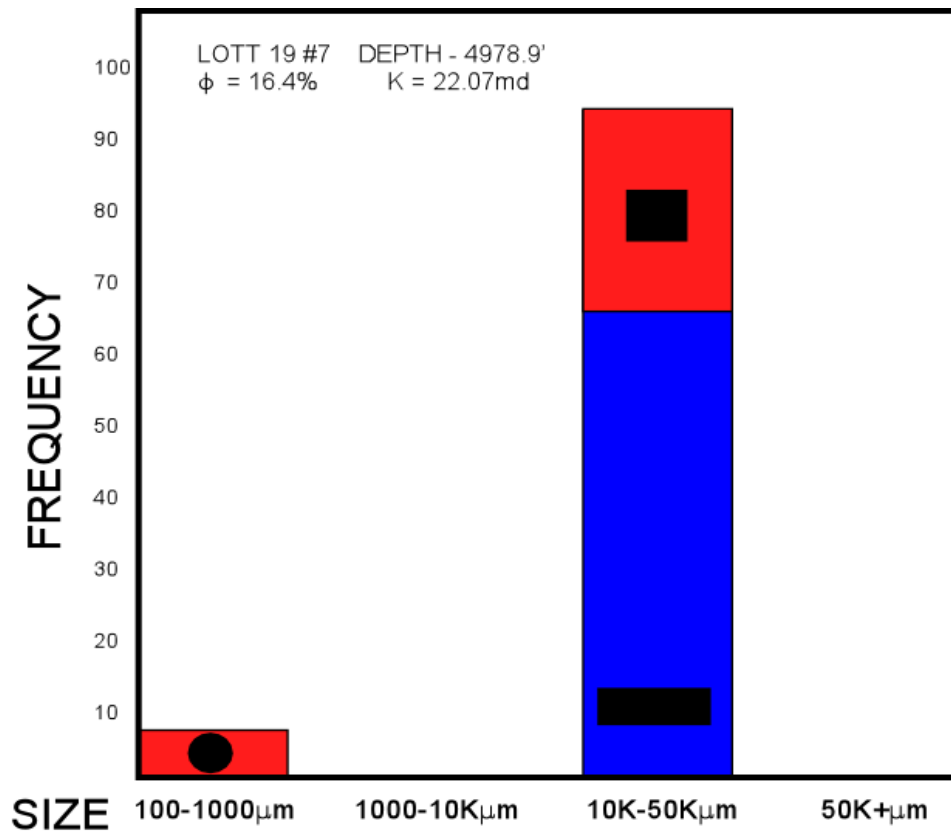
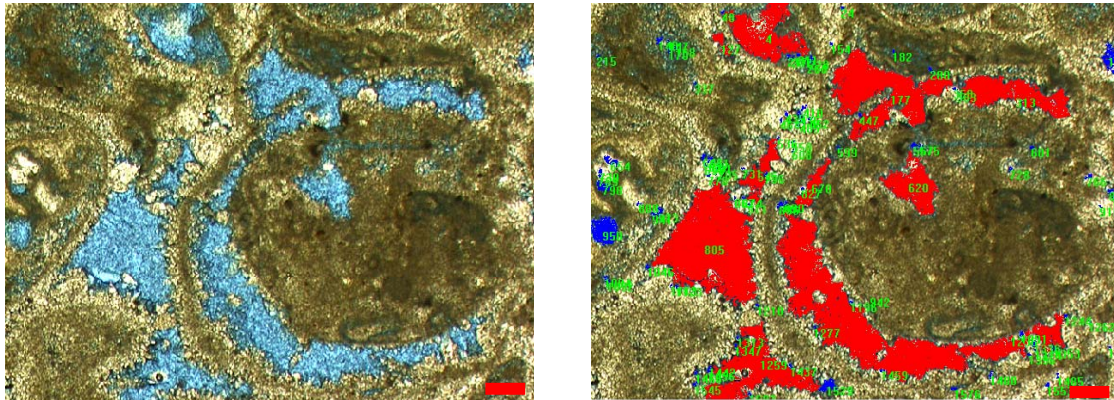


Figure 26. Lott 19 #7, 4978.9' photomicrographs and histogram. Large molds and solution enhanced intergranular pores occupy 90% of total pore volume in the best pore facies.

Intermediate quality pore facies are present in moderately cemented skeletal grainstones and packstones. An example of this pore facies is present in the Lott 19 #7 well, 4981.2' (Figure 27). Dominant pore types are incomplete moldic and solution enhanced intergranular. A component of solution enhanced intergranular pores is also common. Porosity is typically 15-25% and permeability ranges from 5-12 md.

The lowest quality pore facies is comprised of two sub-pore facies. The first includes isolated molds that are present in highly cemented oolitic skeletal grainstones (Figure 28). The leaching was only effective on metastable grains and little else underwent micritization, stabilization, and neomorphism. As a result of this, the pores are often isolated, unconnected, and would be classified as non-touching vugs (Lucia, 1983). Cumulative frequency histograms of this pore facies are typified by large amounts of large molds, and less than 10% of any other pore type or size. Porosity averages 10-14%, but may reach as high as 25%. Permeability is typically less than 5 md.

The overall lowest quality pore facies is present in silty, skeletal packstones, siliciclastic siltstones, and rudstones (Figure 29). Typically, porosity is less than 10% and permeability is less than 10 md. This rock type will have a considerable amount of quartz present that aids in the large proportion of solution enhanced intergranular porosity commonly found. Large, blocky vugs are also typical of this pore facies. Hammel (1996) established a quality classification of flow units incorporating porosity and permeability pairs. The relative quality of pore facies identified with PIA was compared with intervals of Hammel's "best, intermediate, and worst" and showed

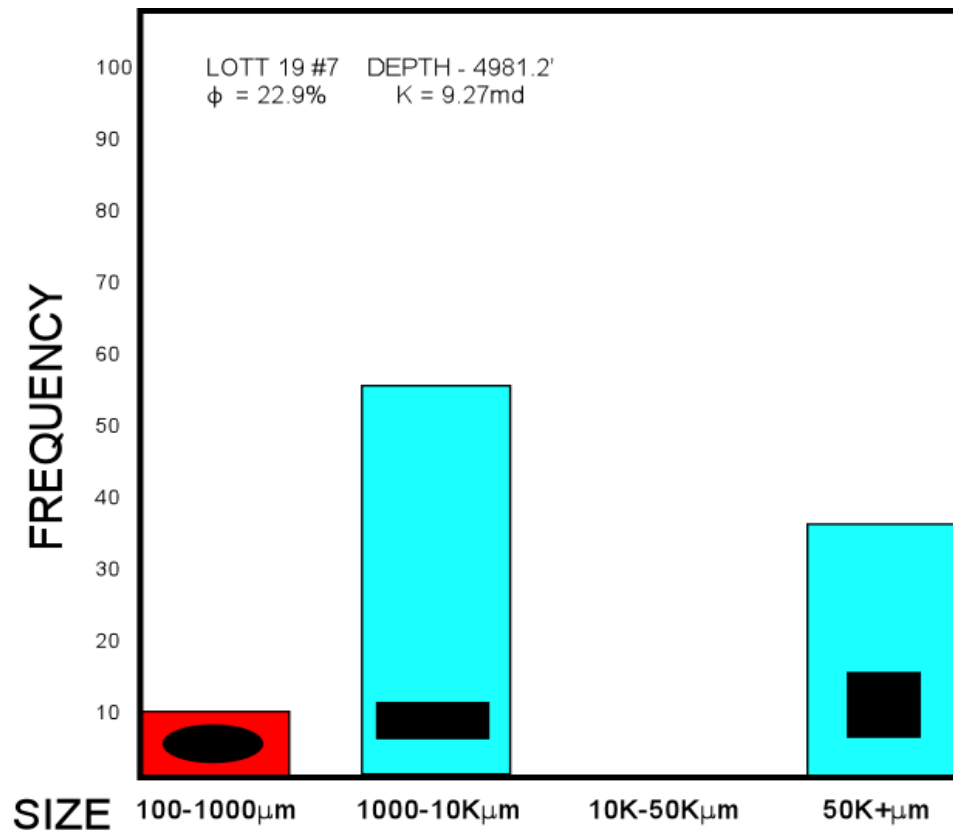
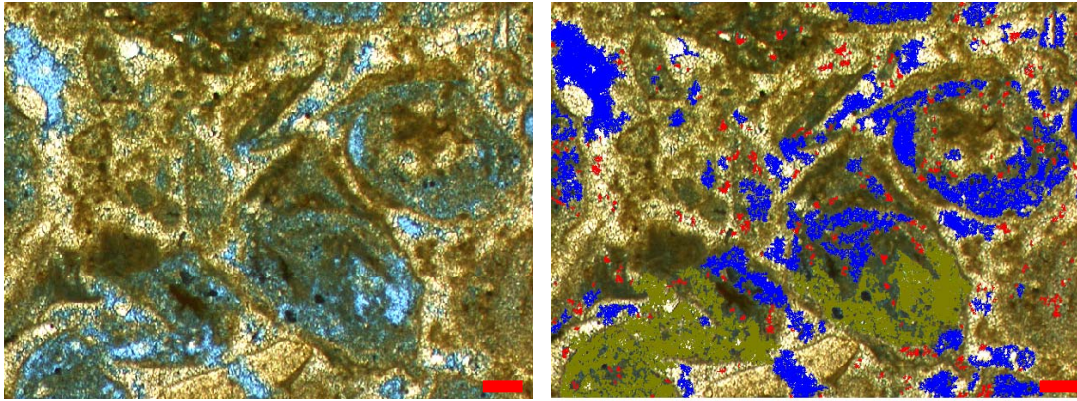


Figure 27. Lott 19 #7, 4981.2' photomicrographs and histogram. Intermediate pore facies where incomplete moldic porosity dominates with occasional, minor complete moldic. A component of solution enhanced intergranular porosity is also common.

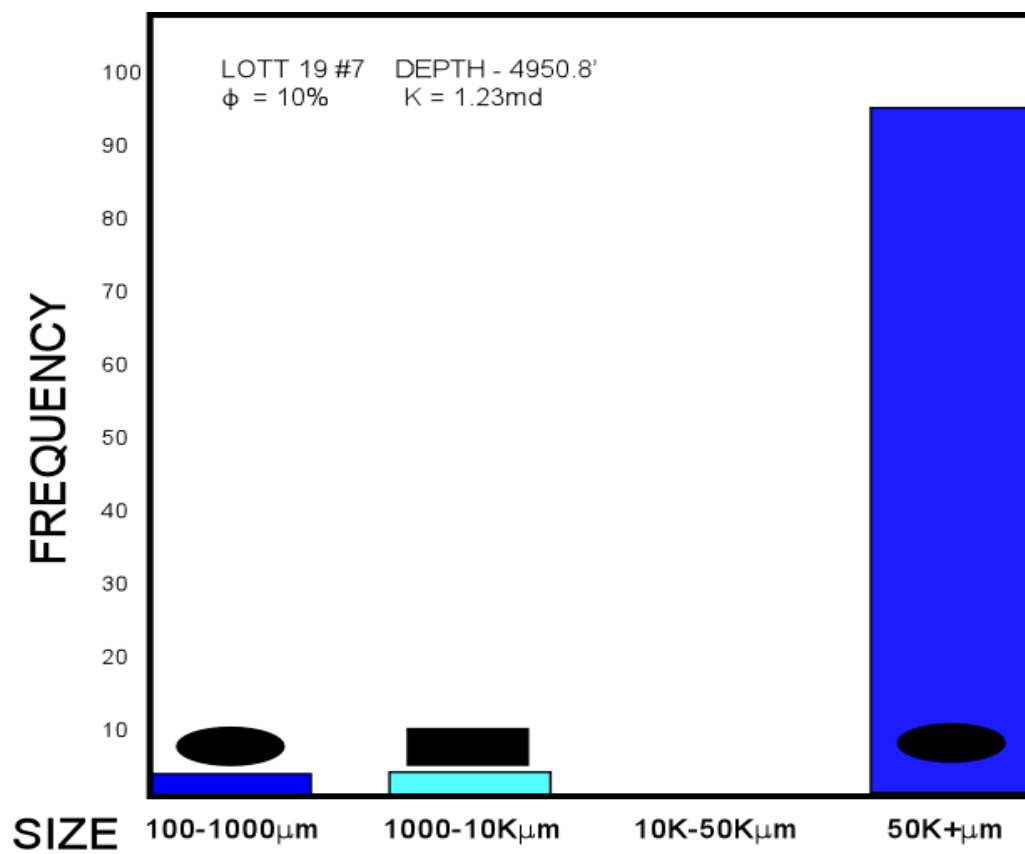
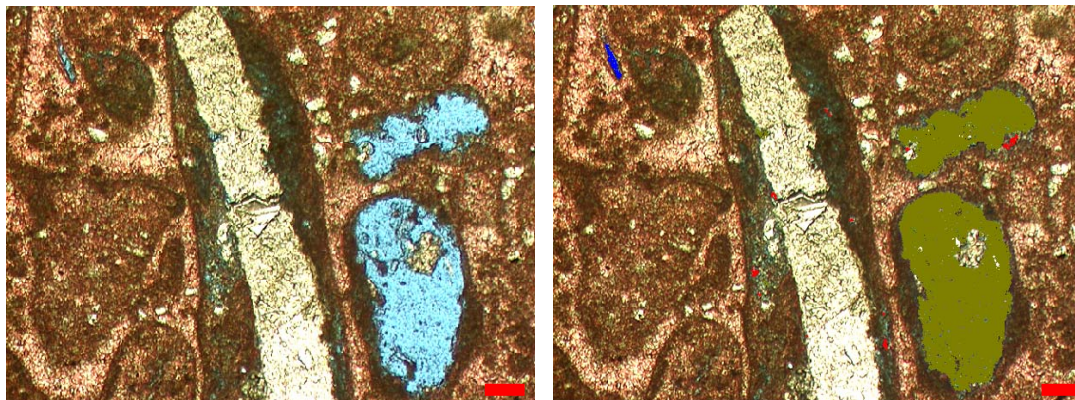


Figure 28. Lott 19 #7, 4950.8' photomicrographs and histogram. The dominance of large moldic pores and the lack of any other substantial pore constituent indicate isolated character of porosity.

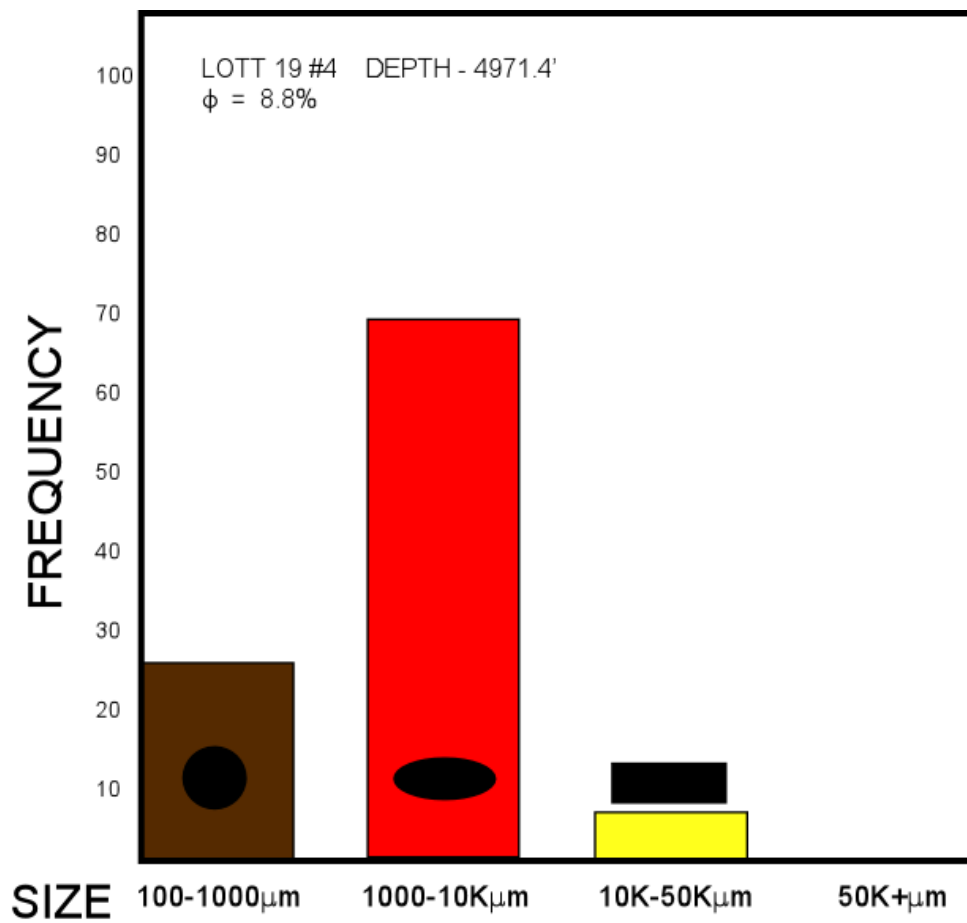
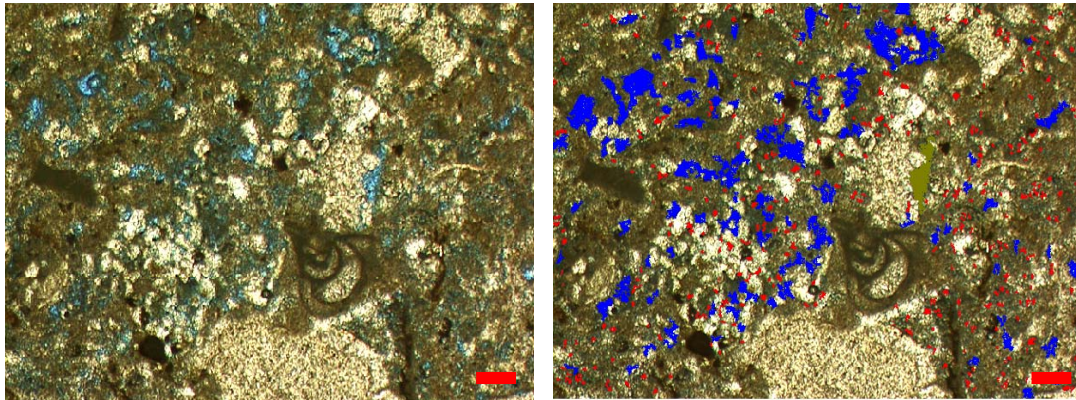


Figure 29. Lott 19 #4, 4971.4' photomicrographs and histogram. The typical signature of this pore facies was the combination of solution enhanced intramatrix and intergranular pores. Blocky, vuggy porosity was also common.

good correspondence. Discrepancies that arose are attributed to the fact that Hammel averaged poro-perm pairs over intervals of ten feet, whereas four or five samples may have been analyzed by PIA in the same interval. The four major pore facies identified may only represent broad templates. The summation of pore facies data (Figure 30) represents patterns and trends to carbonate pores at Happy field and are offered as such. Variations of pore character will occur as a result of diagenetic inconsistencies and sedimentological variations. But as calibrated, field samples are expected to adhere to this scheme.

Mercury Injection Capillary Pressure (MICP)

Background

An additional ten thin sections were analyzed by PIA and standard petrographic methods. Ten plugs were taken by Ahr (pers. comm.) from representative lithofacies across Happy field. Frequency histograms of pore data were generated as in the previous method. In this facet of the study, MICP data of the ten samples was compared to pore geometry. Median pore throat diameter was compared to various pore characteristics. Ehrlich et al. (1991) addressed this issue in siliciclastics where pore type and geometry led to the prediction of pore throat size and in the development of MICP curves. Work on carbonates has included Wardlaw (1979), where pore geometry and recovery efficiency was related to pore to pore throat ratios. Pore casts were examined in the effort to characterize pore and throat geometry's and to better understand capillarity of carbonates (Wardlaw, 1976).

The MICP portion of the study was concerned with determining if a relationship existed between pore data obtained from PIA and median pore throat diameters from MICP tests. Though different wells and depths were sampled compared to the pore facies data, the ten samples were in accordance with the pore facies model already established. Pore throat size frequency, median pore throat diameter, porosity, and permeability of each sample was known from MICP analyses (Figure 31). MICP curves also provide data on pore throats in that they are cumulative frequency plots of pore throat size distribution.

	FREQ.	BIN	SIZE(μm^2)	SHAPE	TYPE	ϕ	K
WORST	85+%	1	100-1K	Circular	MAT	0-10%	0-10MD
	10%	2	1K-10K	Elongate	SEIG		
		3	10K-50K	Blocky	V		
WORST	80-90%	3,4	>10K	Elliptical	M	10-20%	0-10MD
	10-20%	1	100-1K	Elongate	SEIG,IM,MAT		
INTER.	60-90%	2,3	1K-50K	Elongate	M	15-25%	5-12MD
		1,4	<1K,>50K	Blocky	IM		
BEST	10-30%	1	100-1K	Elliptical	SEIG		
	75-90%	3,4	>10K	Elongate	M,IM	15-25%	12-25MD
	20-30%	1-3	100-50K	Elliptical	SEIG		

Figure 30. Summary of PIA data. Data summation of the four pore facies identified at Happy field includes pore frequency, bin/size, shape, type, as well as porosity and permeability intervals expected with specific pore facies.

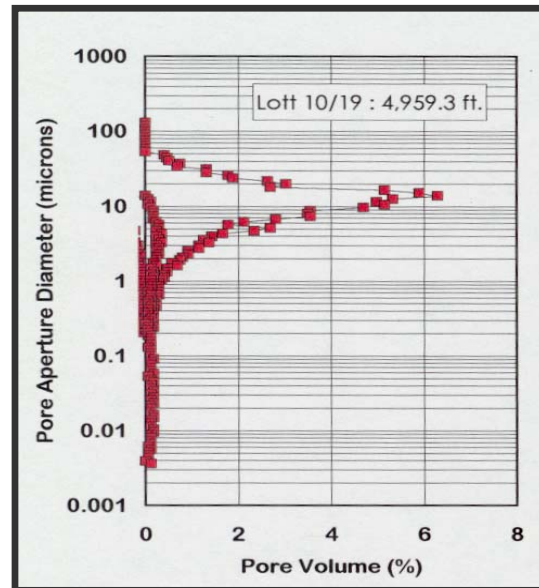


Figure 31. Pore throat size distribution. This plot shows the relative abundance of pore throat sizes within this sample. As is evident by the spike, the majority of pore throat diameters are approximately 10 microns in size.

DISCUSSION

This study focused on two main questions: 1) Can porosity values obtained from image analysis accurately estimate porosity values from other methods, such as core analyses, wireline logs, and standard petrographic analyses? and 2) Can pore data obtained from petrographic image analysis serve as a rapid method to identify reservoir quality, both with a pore facies model and MICP data?

Total Porosity

Reservoir quality depends on the relationship between porosity and permeability. Typically, the most reliable measurements of porosity and permeability are made on core samples. Alternatively, wireline log derived porosity may be related statistically to core permeability. Close correlation between porosity and permeability measurements is characteristic of a simple, intergranular porosity network. This simple pore network does not exist at Happy field, which exhibits pores that have undergone extensive fabric-selective diagenesis. Thus a close correlation of porosity and permeability values is also nonexistent. Semi log plot of porosity vs. permeability shows poor correlation (Figure 32), suggesting predictions of permeability from total porosity values are unreliable. This is a common predicament when dealing with carbonates that contain several pore types and sizes and are not related to permeability by a simple, linear equation.

In order to find a method to relate porosity and permeability to reservoir quality, values of porosity and permeability were paired for each sample and paired values were grouped into highest, intermediate, and lowest combined values. These ranked porosity

and permeability values were used as reservoir quality indicators. Common pore characteristics from PIA data were then determined for samples of equal quality. This method established the pore facies model discussed in RESULTS (p. 45) where pore attributes aid in the prediction of petrophysical behavior and reservoir quality. However, porosity and permeability pairs can be related to specific lithofacies within the field, as each lithofacies has a characteristic “porosity fingerprint”. This indicates that bracketed values of porosity and permeability would be expected with certain rock types within the field. As indicated by Figure 33, lithofacies with pore attributes in common plot as fields of similar porosity and permeability values. For example, oolitic grainstones exhibit the highest poro-perm values, and are the highest quality reservoir rocks in the field as a result of the abundance and specific combinations of pore types and sizes.

Porosity values obtained by core analyses, standard petrographic methods, and wireline logs were compared to values obtained from PIA. This was done by comparing core porosity with porosity from standard petrographic analyses in order to compare measured porosity values. The good correlation between core porosity and petrographic porosity (Figure 34) indicates that porosity measured as 2D images corresponds well with measured core porosity. Total porosity in each sample was determined by image analyses and was compared with porosity obtained by standard petrographic methods. This comparison established that porosity from standard petrography which is measured across the entire thin section correlates well with PIA porosity which is obtained from a series of points on each thin section sample. All image analysis measurements were conducted using identical magnification for each pore size range. Figure 35 illustrates

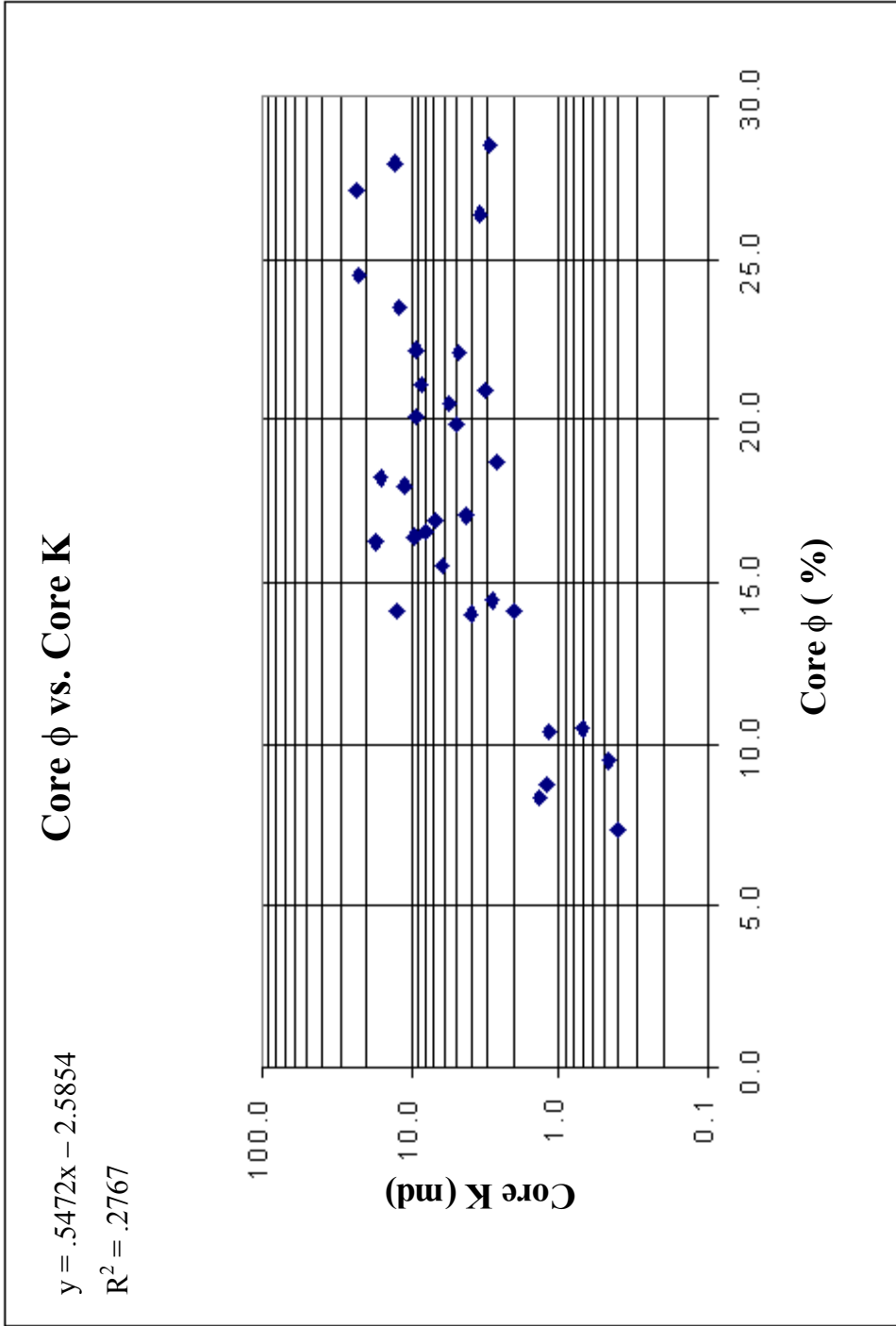


Figure 32. Core porosity vs. core permeability. This shows total porosity measured with all pore types and sizes included.

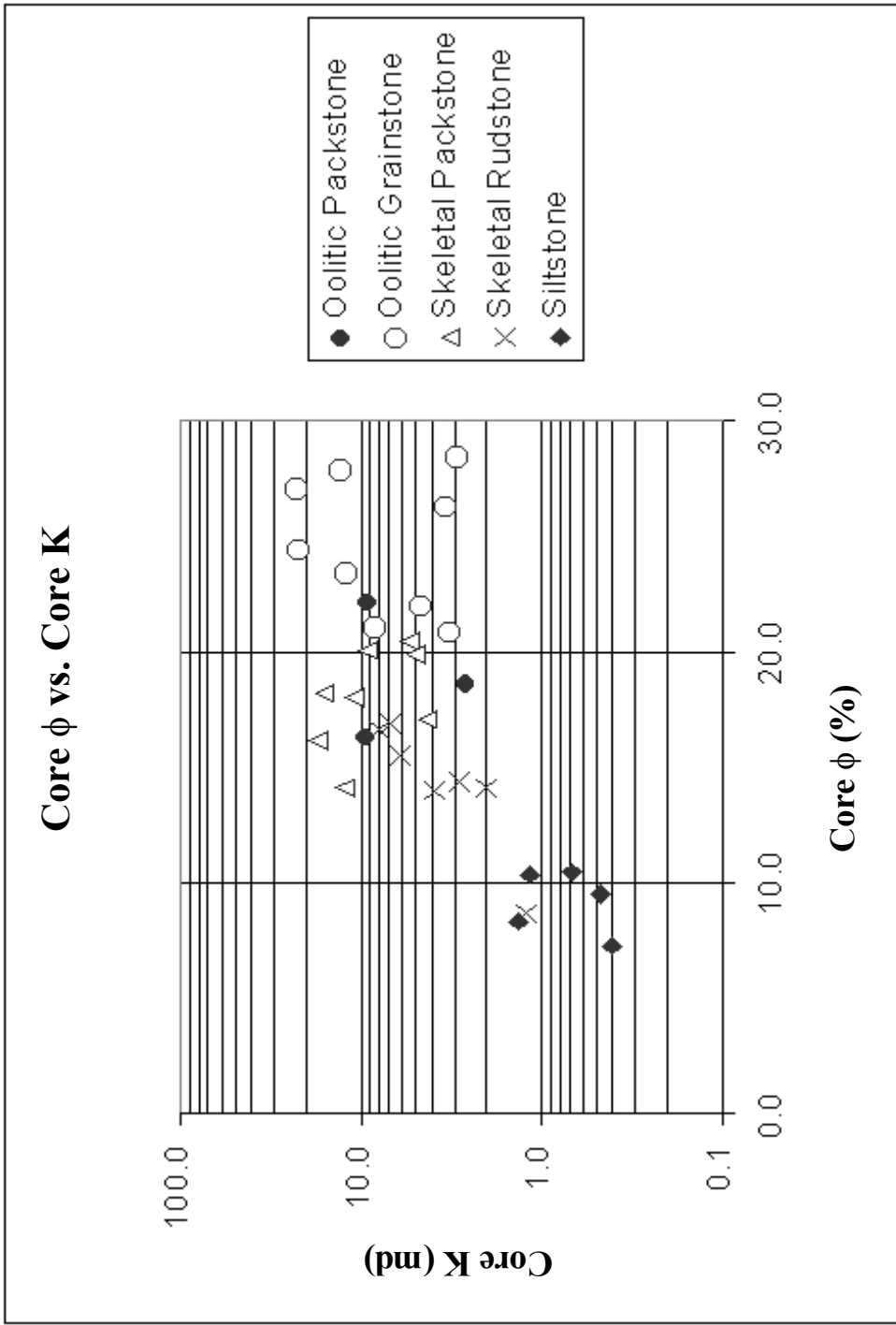


Figure 33. Core porosity vs. core permeability with lithofacies. Note that similar lithofacies plot in common fields where oolitic grainstones exhibit the highest poro-perm pairs.

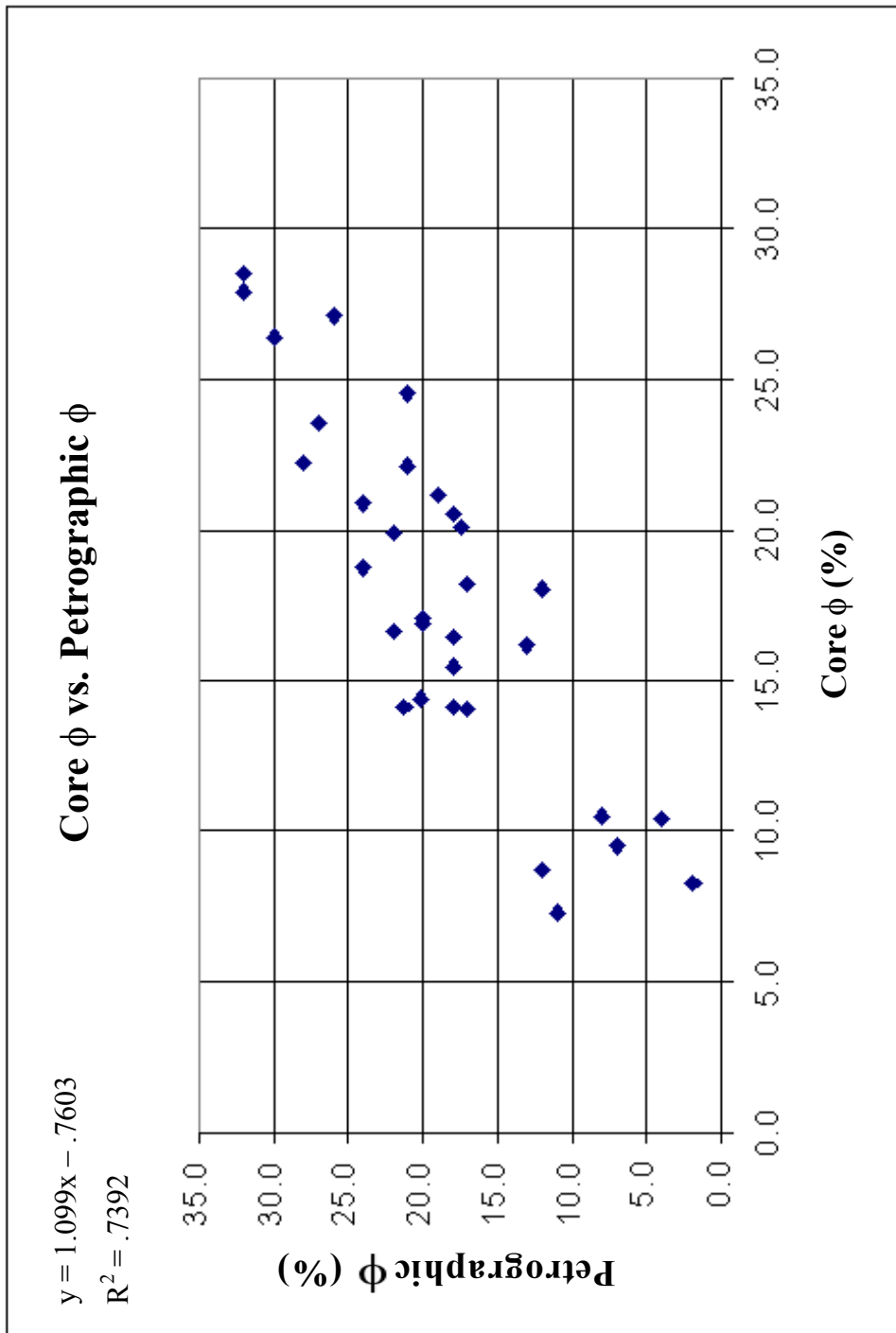


Figure 34. Core porosity vs. petrographic porosity.

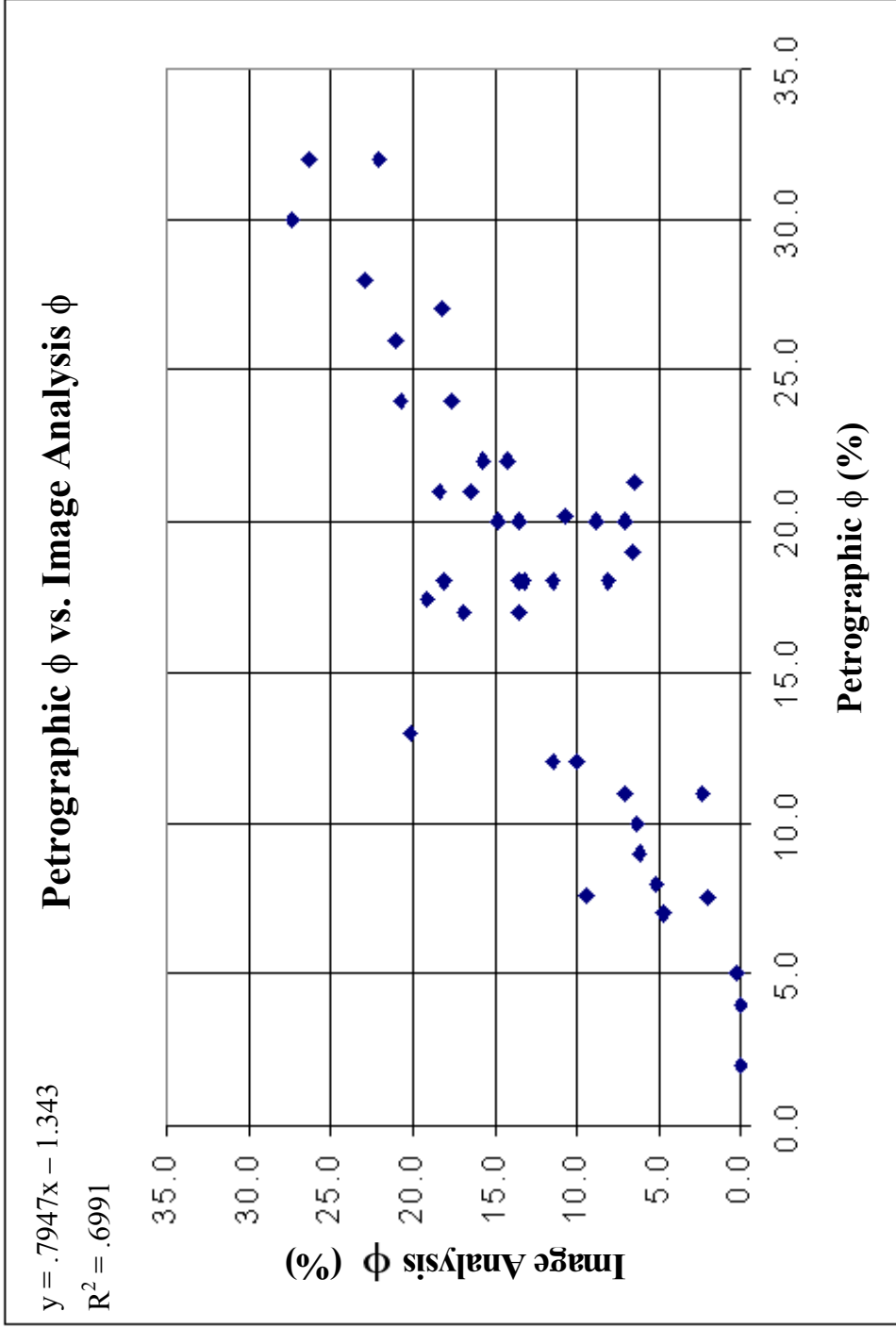


Figure 35. Petrographic porosity by standard methods vs. image analysis porosity. Note, that PIA methods typically underestimates visual porosity between 3-5%.

the correlation between visual estimates of porosity from PIA and standard petrography. As the graph suggests, PIA methods will typically underestimate total porosity as compared to standard petrography. This may be explained by two reasons. The choice of magnification for PIA has great bearing on the amount of porosity present in an image. The porosity imaged and measured is dependent on the size of the field of view. High magnification may focus on a single pore occupying the entire field of view resulting in exaggeration of porosity measured. Magnification that is too low does not identify small pores precisely and reliably resulting in porosity values less than expected. The reliability of porosity values obtained from PIA as compared to porosity from core analyses is shown in Figure 36. This plot shows that porosity percent from PIA underestimates porosity from core analyses. However, the high correspondence between data types suggests the method of determining porosity from PIA is relatively accurate, and can serve as a simple transform to substitute for measured porosity in core analyses.

Wireline logs were analyzed to determine porosity. Neutron porosity and density porosity logs were analyzed for porosity values and then a corrected porosity value was determined using both curve values and depending on mud type (Asquith, 1997). Figure 37 shows this relationship. Again, porosity measurements from PIA typically underestimate wireline log values of porosity.

Porosity obtained from all methods plotted against depth is shown in Figure 38. The plot indicates that porosity obtained from PIA typically underestimates porosity compared to porosity obtained by alternate methods. There is good agreement between the porosity values and a similar trend of data points.

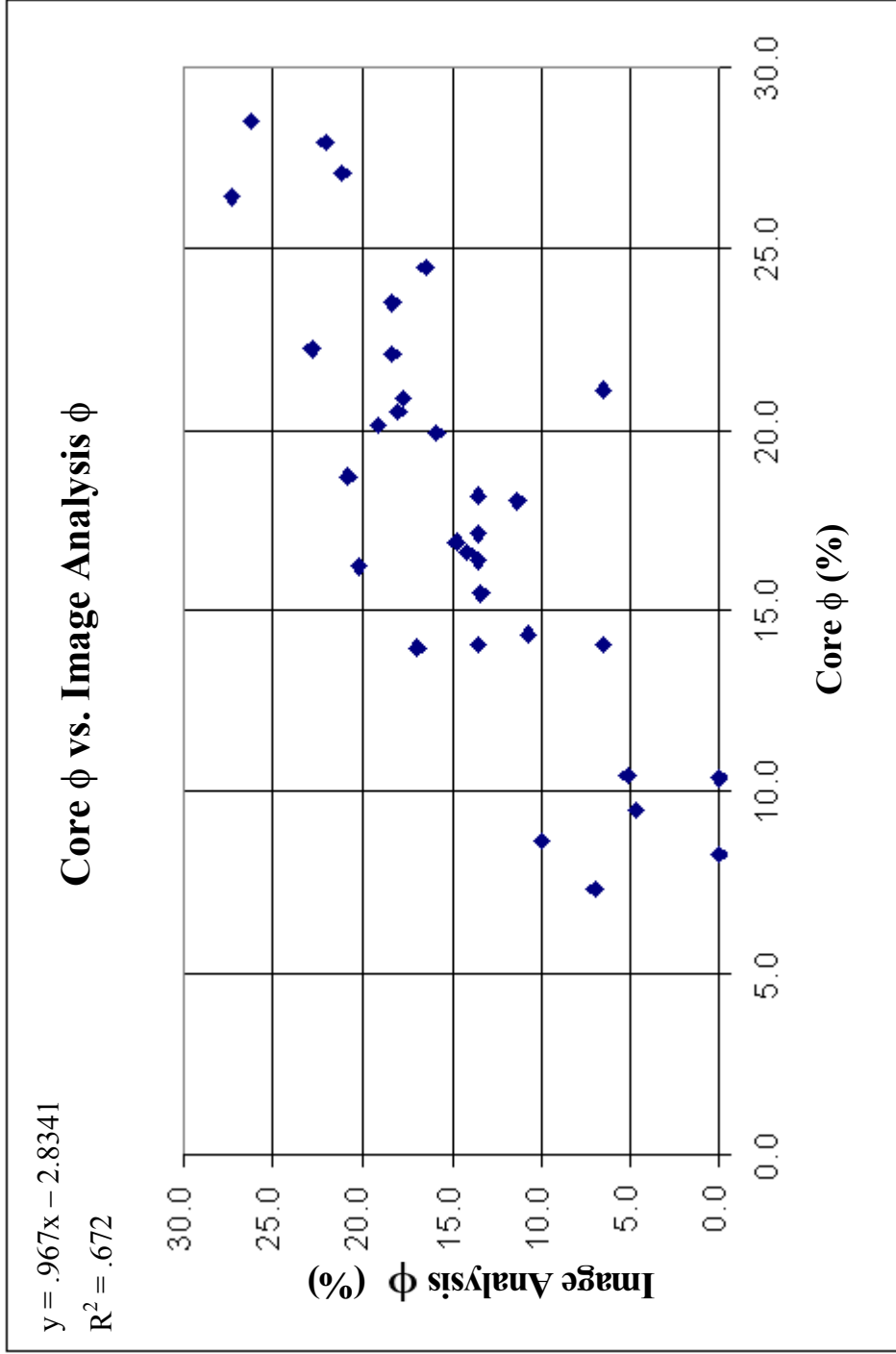


Figure 36. Core porosity vs. image analysis porosity. This plot shows total core and PIA porosity which includes all pore types and sizes.

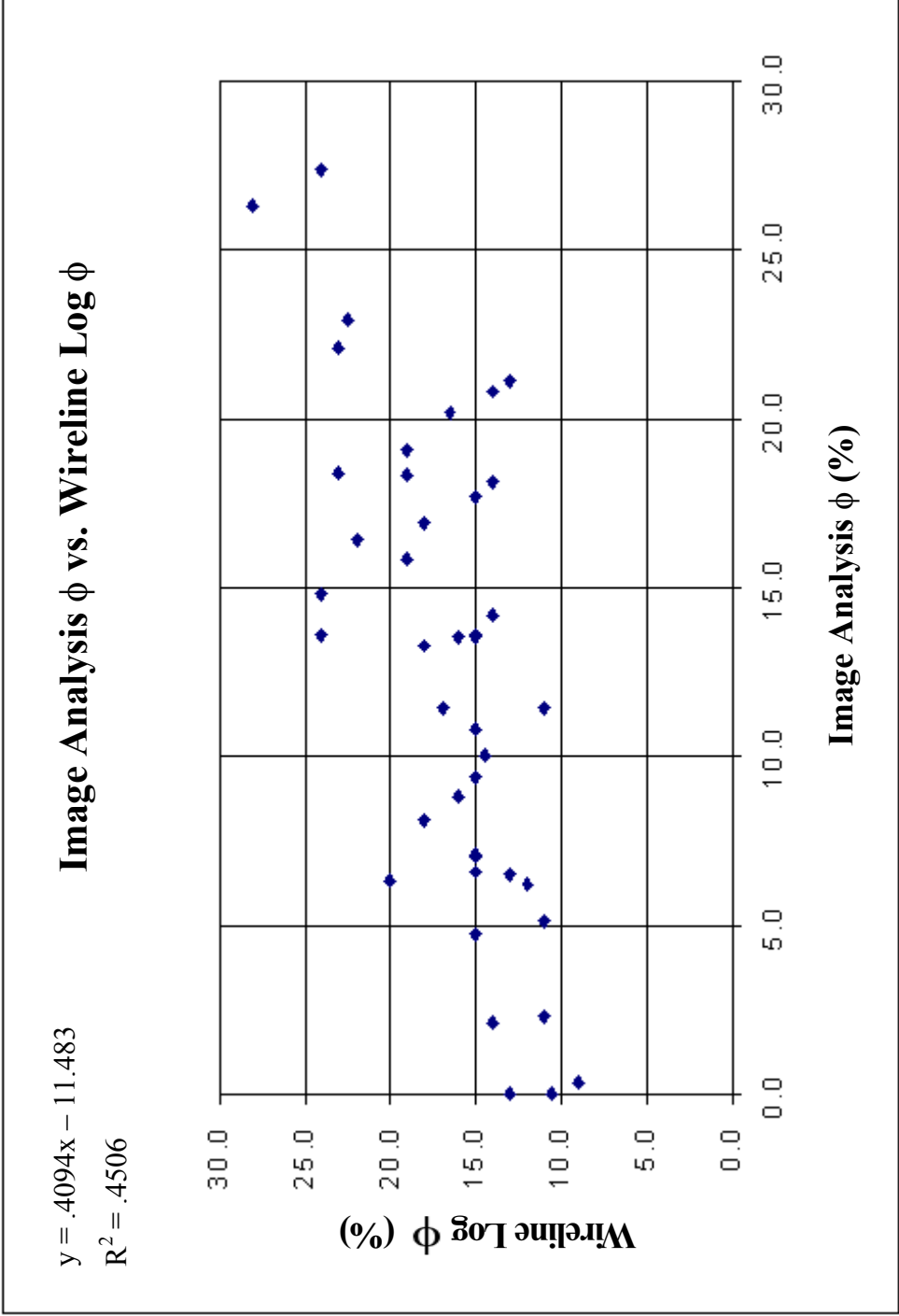


Figure 37. Image analysis porosity vs. wireline log porosity. Image analysis consistently underestimated wireline log porosity by 2%-4%.

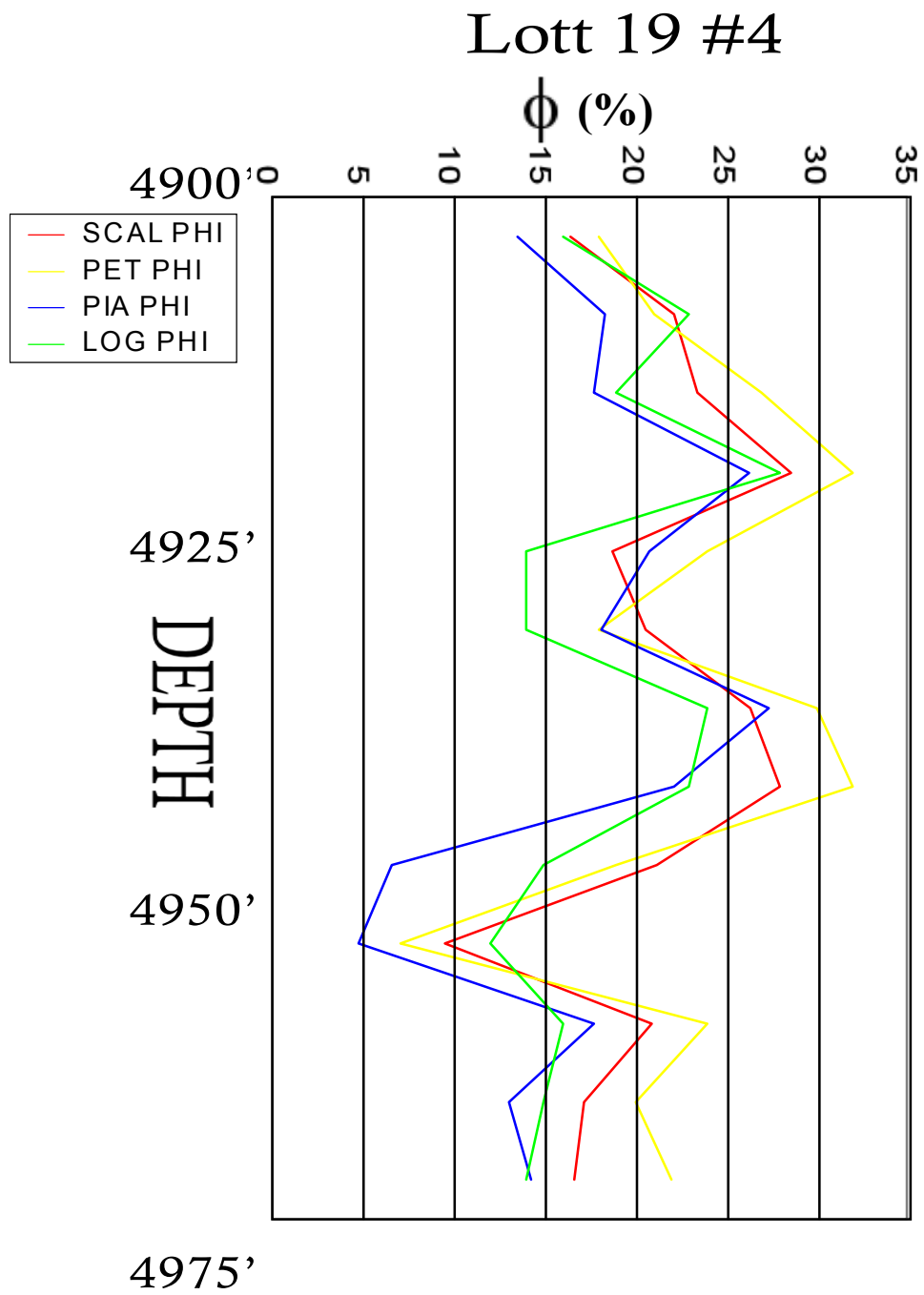


Figure 38. Lott 19 #4 well porosity comparison. SCAL = core analyses, PET = petrographic methods, PIA = petrographic image analysis, and LOG = log porosity. Log and PIA porosity were commonly underestimated compared to core analyses values.

Pore Data and Pore Facies

The pore facies model that was developed in the previous chapter is based on pore data from PIA as an indicator of reservoir quality. Pore data includes pore size, shape, origin, frequency (relative abundance), and total abundance of porosity. The purpose is to determine whether pore data provides a reliable classification system for reservoir quality.

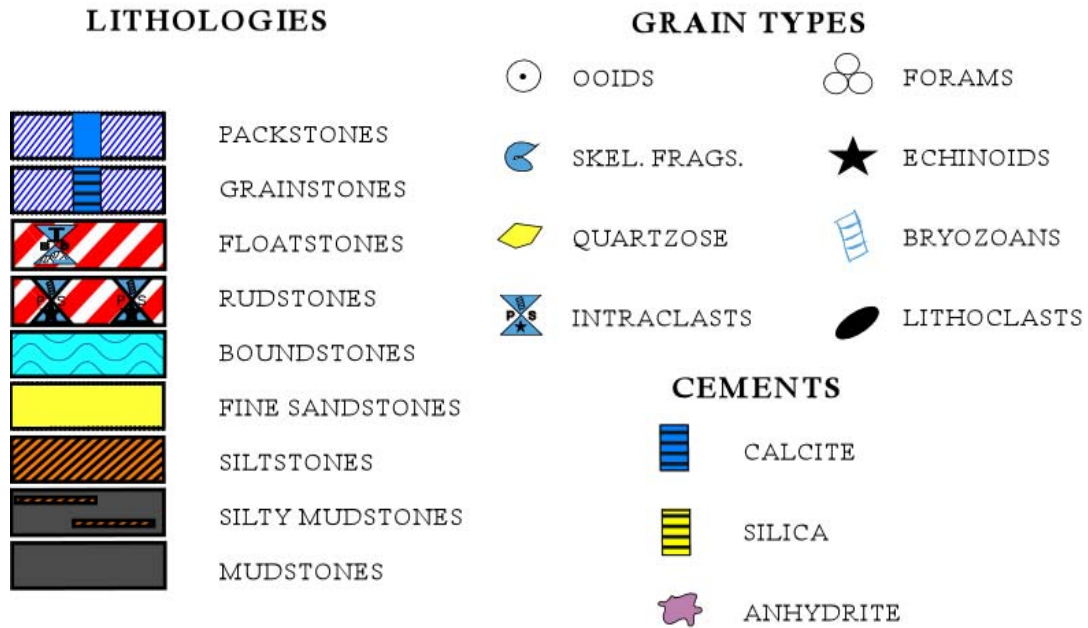
The pore facies model was developed from pore data obtained and interpreted from PIA methods. That data enabled a classification system to be created. Pore facies were then identified, classified, and ranked according to pore attributes and assessed as to relative quality. This system was compared with Hammel's (1996) method where reservoir quality is based on paired values of porosity and permeability. For example, high poro-perm paired values are indicative of high quality reservoir rocks and low poro-perm paired values are indicative of low quality reservoir rock. His classification scheme resulted in six quality ranks that include the entire range of permeability values at Happy field. The 3D architecture of the flow units was then established within Happy field. The architecture is illustrated in Figure 28 (Hammel, 1996) which shows flow units that were identified by poro-perm pairs in well bores and then correlated across the field.

Hammel's (1996) work, however, did not include attributes and properties of pores. Also, it failed to determine the correlation between porosity measurements obtained by various methods, namely standard petrography and core analyses. Furthermore, total porosity comparisons were not evaluated to determine trends in

porosity values obtained, nor was total porosity subdivided into pore components to determine relation of pore data to reservoir quality. This study by contrast focuses on determining whether image analysis could accurately measure total porosity for comparison with porosity values measured by other techniques. These techniques include core analyses, standard petrographic techniques, and determining porosity from wireline log analysis. Also, this study focused on dissecting the entire porosity complex into components of size, shape, origin, and relative abundance and then to utilize the data in developing a reservoir quality classification system.

Figure 39 is the legend for Figure 40. Figure 40 is a stratigraphic cross-section of Happy field showing the flow unit architecture based on reservoir quality by pore facies model developed from PIA data (Figure 30). This was compared with the findings of Hammel (1996), most notably, Figure 28, to compare high and low quality intervals in both systems. Good correspondence between intervals of comparable quality was observed throughout the field. For example, Hammel (1996) identified an oolitic grainstone interval with high poro-perm pairs in the Lott 19 #4 well. The same grainstone “sweetspot” was also identified by the pore facies model as a high quality section and subsequent correlation of this interval across Happy field resulted in flow unit architecture that was comparable to that of Hammel (1996). The detail of Hammel’s (1996) study was not reached as his model was based on poro-perm values from core analyses which were provided across a 1-foot interval. In this study, the model was based on porosity data from thin-section samples which were, on average, taken across 5-foot intervals.

LEGEND



PORE FACIES

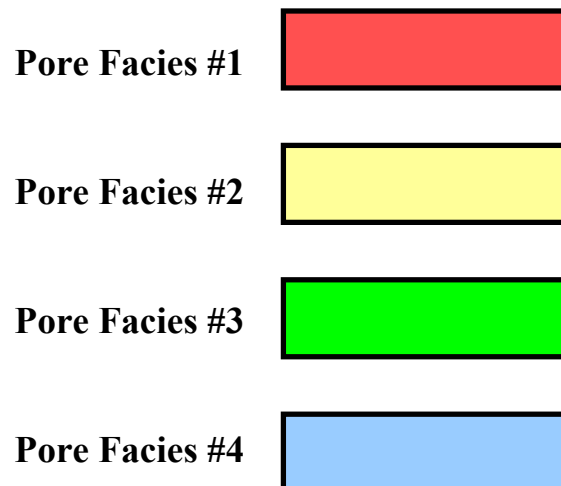
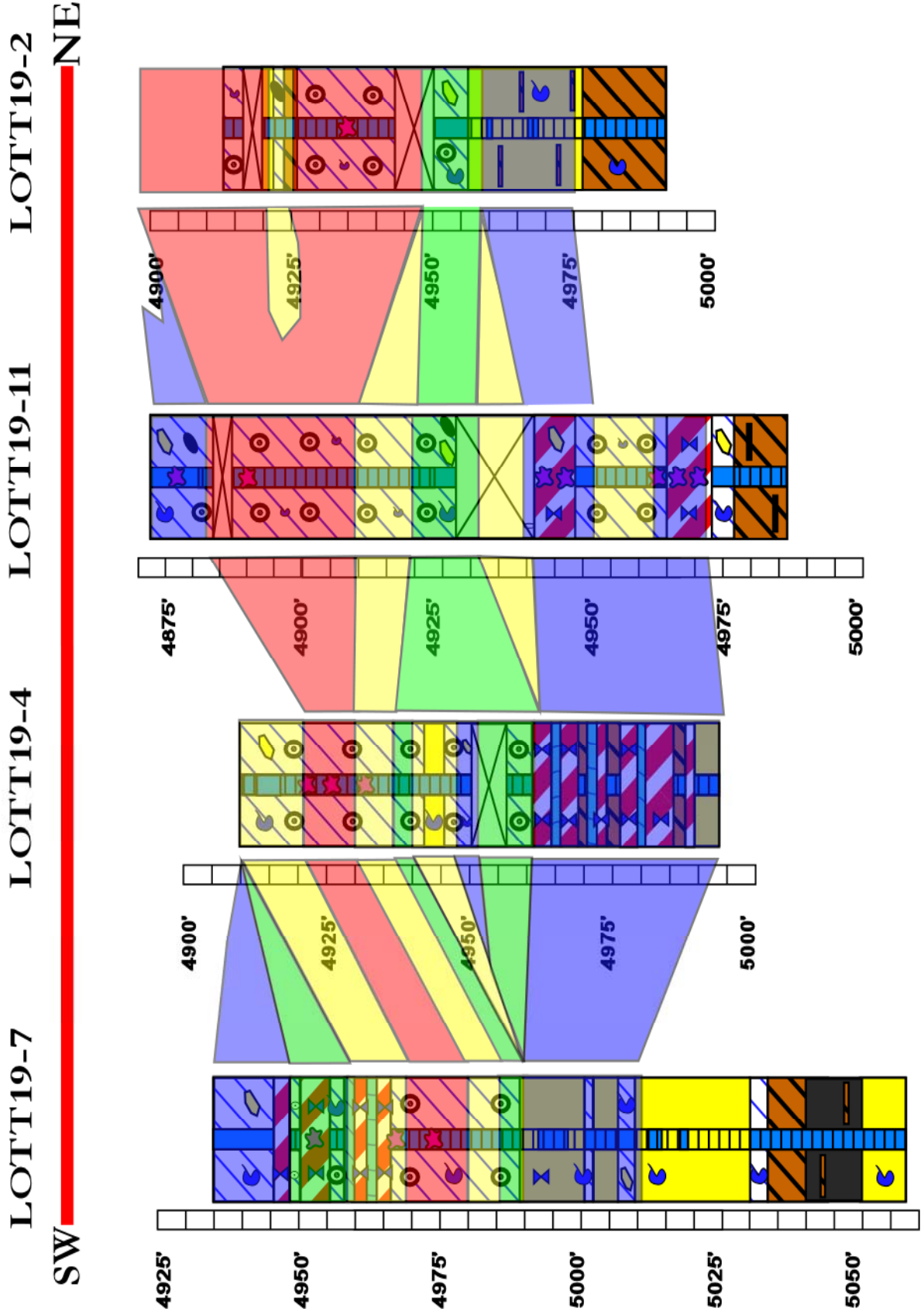


Figure 39. Legend for pore facies model stratigraphic cross-section.

Figure 40. Stratigraphic cross section incorporating pore facies model. Shown is a stratigraphic cross section transecting southwest to northeast. The lithologic well logs show rock type, primary grain constituents, and cements. The intervals of pore facies architecture has been color-coded consistent with the pore facies model summarized on page 54. The highest reservoir quality interval is associated with pore facies #1 (red) which is present in the oolitic grainstone. This interval is suggested to increase in thickness towards the northeast. Also note that the producing interval of pore facies #1 and #2 are typically bounded by non-productive, low quality reservoir rocks of the other pore facies.



Petrographic Image Analysis Predicting Capillary Pressure Behavior

Ten samples were chosen for Mercury injection capillary pressure (MICP) experiments. The samples were chosen to represent good, intermediate, and poor reservoir quality zones based on Hammel's (1996) study. Slices were cut from the plugs prior to injecting with mercury and thin sections were made from the slices. These thin sections were examined by standard petrographic methods and by PIA to determine whether thin section measurements on pores show any correlation to median pore throat diameters (MTD) calculated from MICP data. If good correlation could be found, it would indicate that image analysis data, in the form of median pore size (MPS) could serve as proxies for MTD obtained by expensive and time-consuming MICP analyses.

Permeability depends on pore throat size and geometry. Figure 41 shows a close correspondence between MTD and permeability. A plot of PIA porosity vs. MTD (Figure 42) shows moderate correlation suggesting that MTD less than 2 microns may exist in porosity values ranging from 4%-25%. But a positive relationship exists between the porosity, abundance of pores, and the size of the throats that connect them. Image analysis porosity vs. core K (Figure 43) shows good linearity and moderate correlation, suggesting that porosity obtained from petrographic image analysis techniques is a reasonable predictor of permeability. Table 3 summarizes data obtained from the additional ten thin section samples.

Pore sizes and MTD were compared to determine if MTD correlate with pore size obtained from image analysis methods. In siliciclastics this relationship is typical

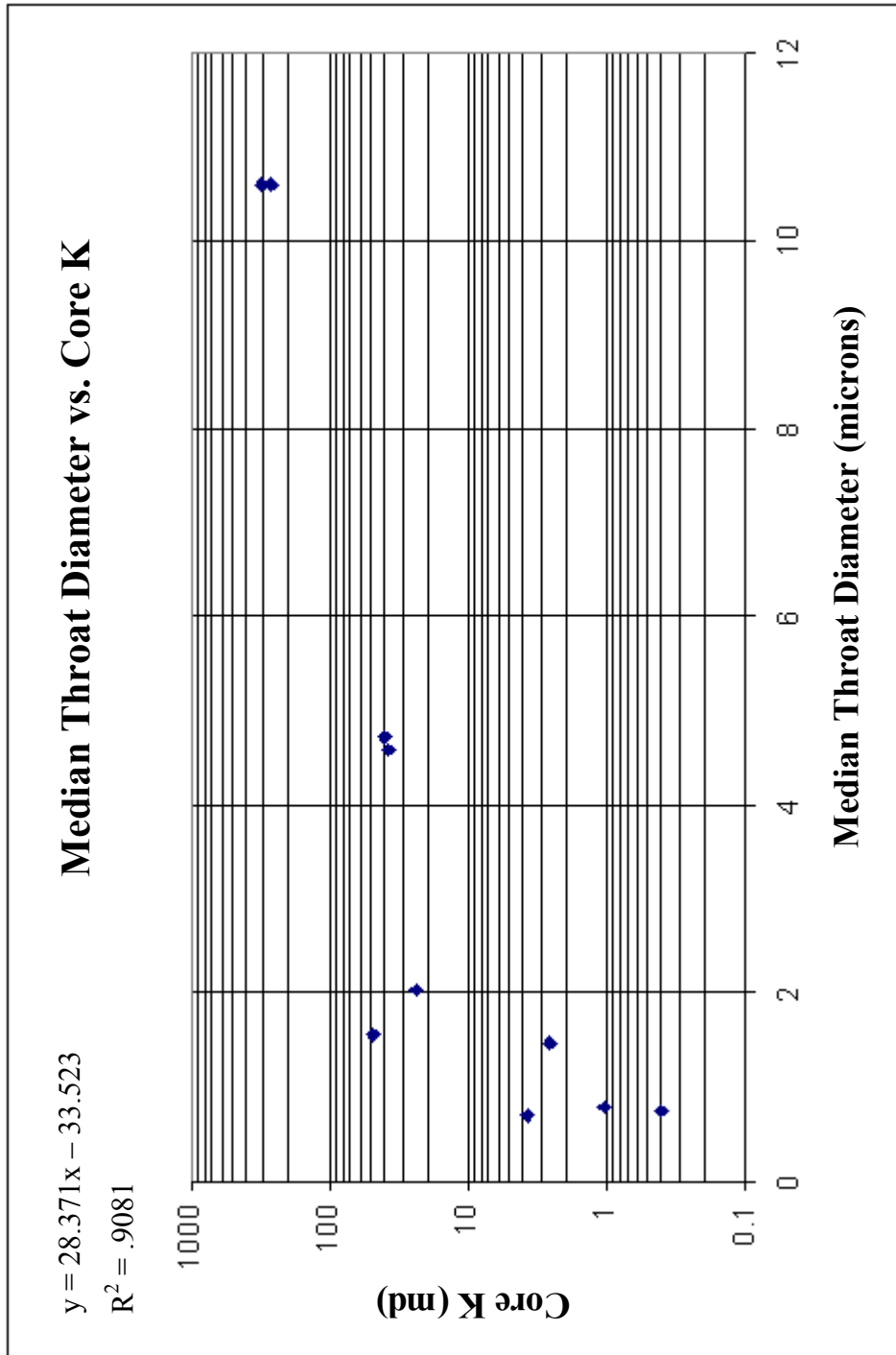


Figure 41. Median throat diameter vs. core permeability. Permeability is most closely correlative to pore throat aperture size, or MTD, and this chart shows excellent correlation with a coefficient of .9081.

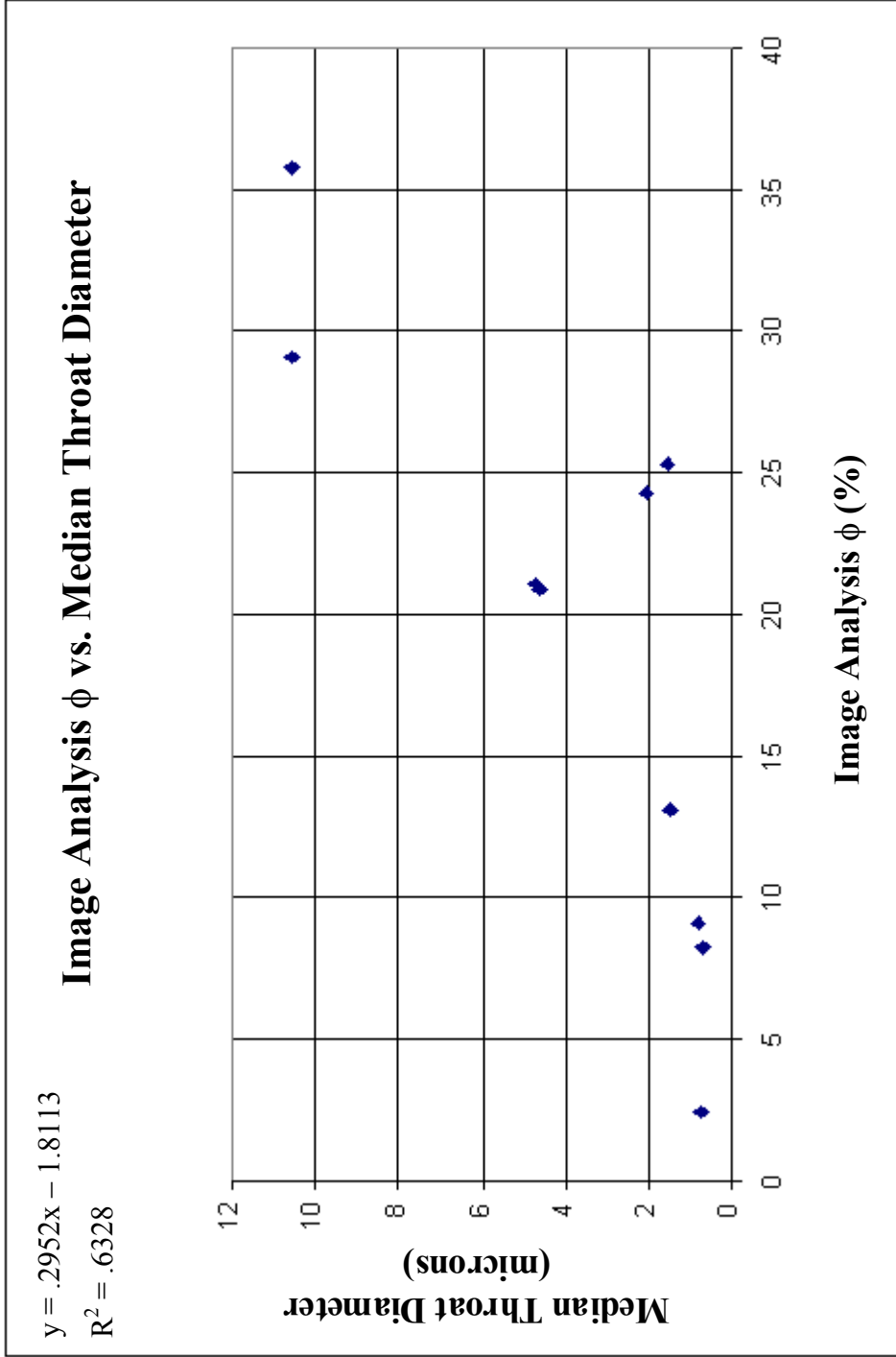


Figure 42. Image analysis porosity vs. median throat diameter. This graph indicates a positive relationship between porosity percent and pore throat size.

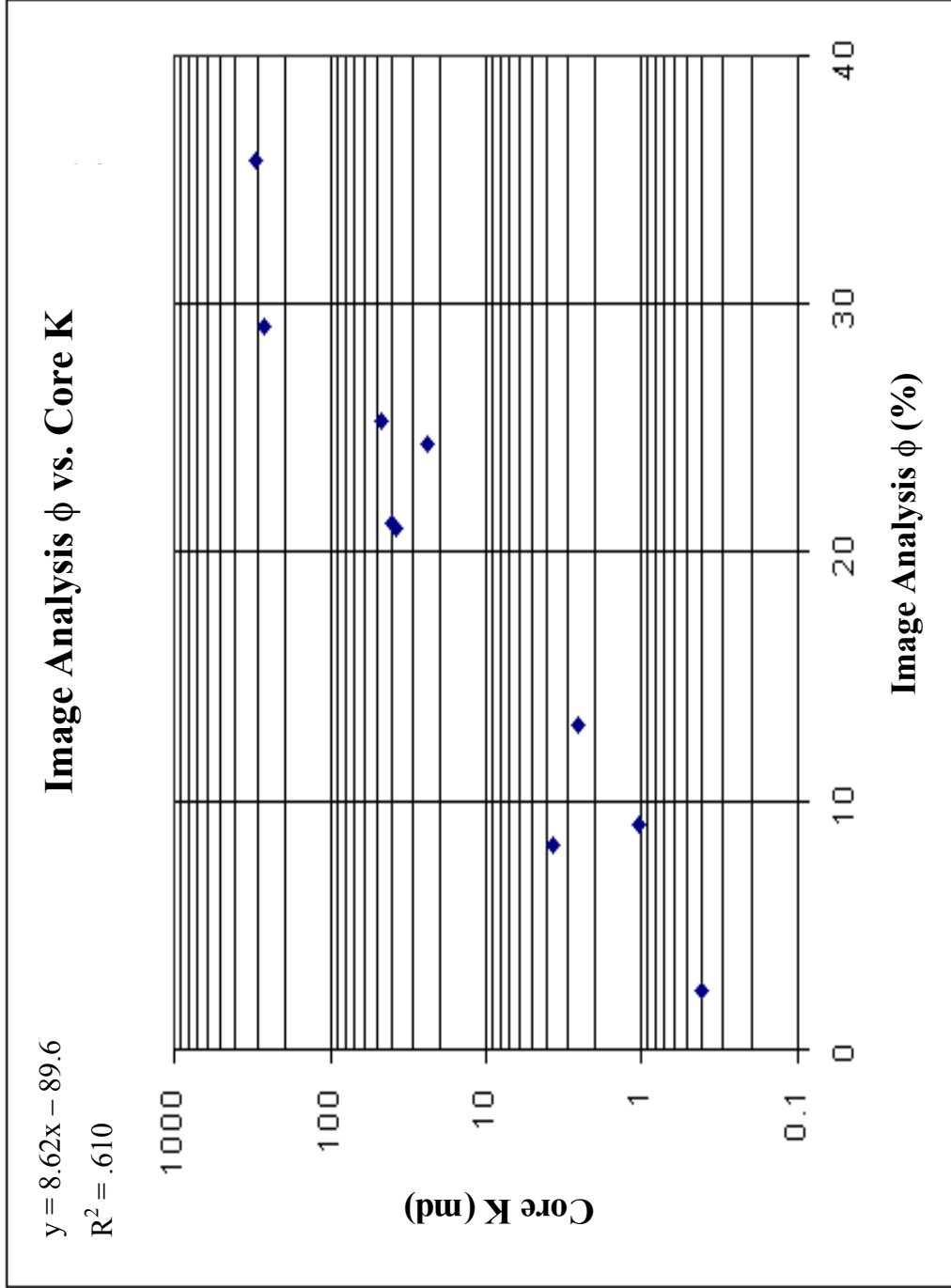


Figure 43. Image analysis porosity vs. core permeability. This graph also shows a positive correlation between porosity obtained from PIA and core permeability.

Table 3. Summary of data from ten additional thin sections. Samples were collected at two different times (Plug Set #1 and #2) and include various lithologies as well as a spectrum of reservoir quality classes. Data includes well location, depth of sample, core porosity, PIA porosity, core permeability, and MTD.

	Slide #	Well #	Depth (ft)	Core ϕ	PIA ϕ	K (md)	MPS (μm^2)	MTD (μm^2)
Plug Set #1	3	Lott 19 #11	4897.5	27.7	29.1	268	207	10.6
	2	Lott 19 #2	4914.0	30.3	24.3	23.7	160	2.04
	7	Lott 19 #4	4924.0	25.5	25.3	48	160	1.55
	10	Lott 19 #11	4941.4	12	9.1	1.03	226	0.783
	1	Lott 19 #5	4959.3	31.3	35.8	311	381	10.6
Plug Set #2	5	Lott 19 #7	4979.0	24.5	21.1	40	301	4.72
	1	Lott 19 #7	4941.5	5.6	2.4	0.402	207	0.742
	2	Lott 19 #4	4943.7	17.2	13.1	2.56	151	1.46
	3	Lott 19 #7	4958.9	14	8.2	3.75	169	0.695
	4	Lott 19 #8	4987.5	20.4	20.9	37.9	738	4.58

because pore size and pore throat size closely relate to sediment grain size. Carbonate porosity is more complex and the relationship between pore size and pore throat size is not as simple. For example, oomoldic pores may be very large and well developed, but may be non-touching, in which case they exhibit anomalously small MTD measurements. The prospect of predicting MTD from MPS measurements from PIA is attractive. Figure 44 shows a plot of MTD vs. MPS. The data show that large pores commonly have large pore throats associated with them. The dominant pore types present at Happy field include oomolds (complete and incomplete), intergranular, and vugs. Of these, vugs exhibit the largest average pore size of 800 square microns, yet they do not have the largest pore throats because many vugs occur in muddy rocks that lack intergranular connectivity. Figure 45 is a photomicrograph of large, non-touching vugs in a skeletal wackestone packstone. This sample exhibits 21% porosity and 21 md of permeability, a moderate quality reservoir rock.

Image analysis can serve as a reservoir characterization tool because pores may be analyzed much more rapidly than with standard petrographic methods. Resulting data on pore size, shape, frequency, origin, and overall abundance is easily obtained, enabling a classification system to be formed based on the pore characteristics. Optimum poro-perm pairs are predicted based on the identification of key pore attributes. These attributes, in turn, are the basis for a classification scheme that estimates reservoir quality.

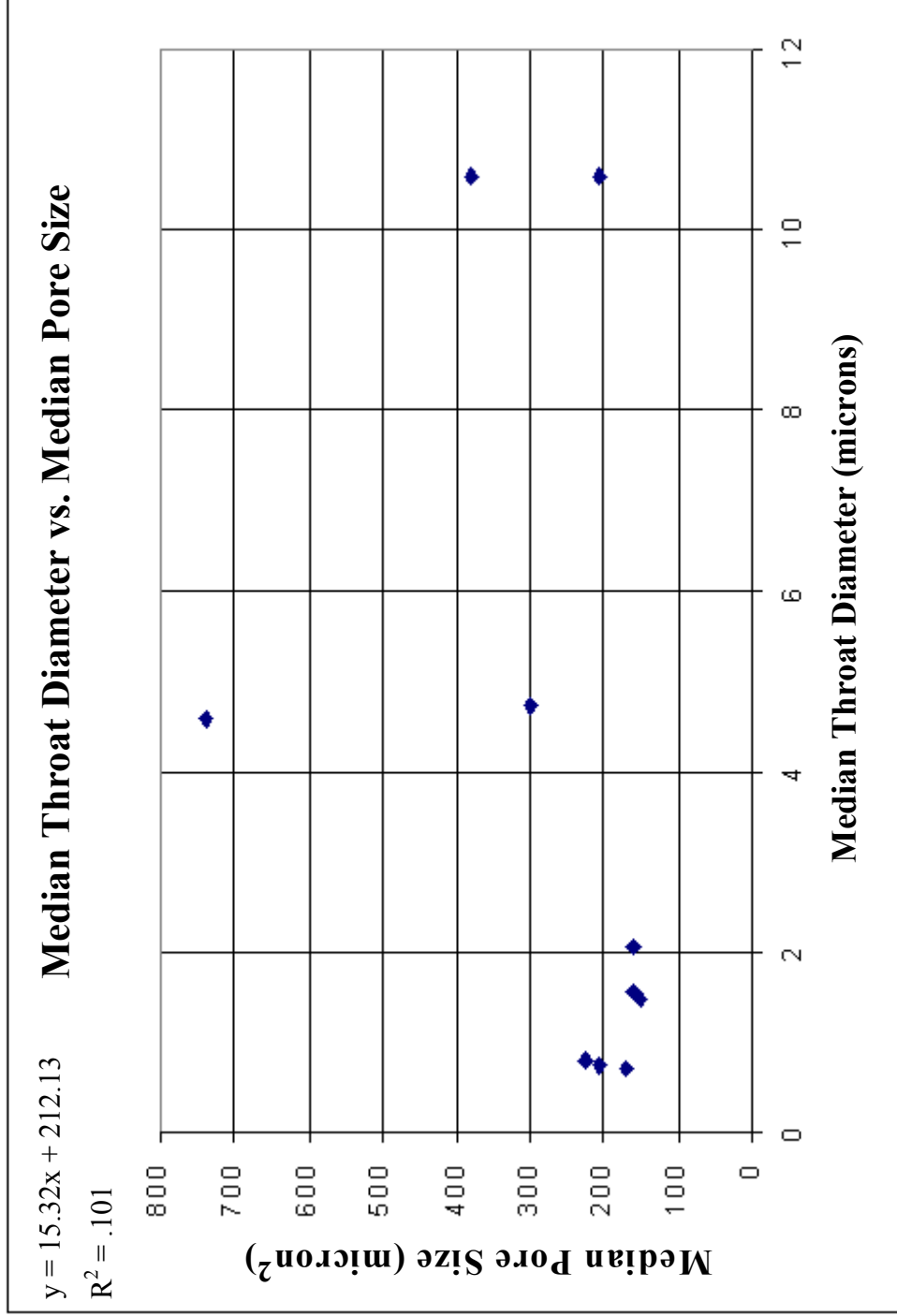


Figure 44. Median pore throat vs. median pore size. A positive correlation is evident and the outlier is a sample with large, isolated vugs.

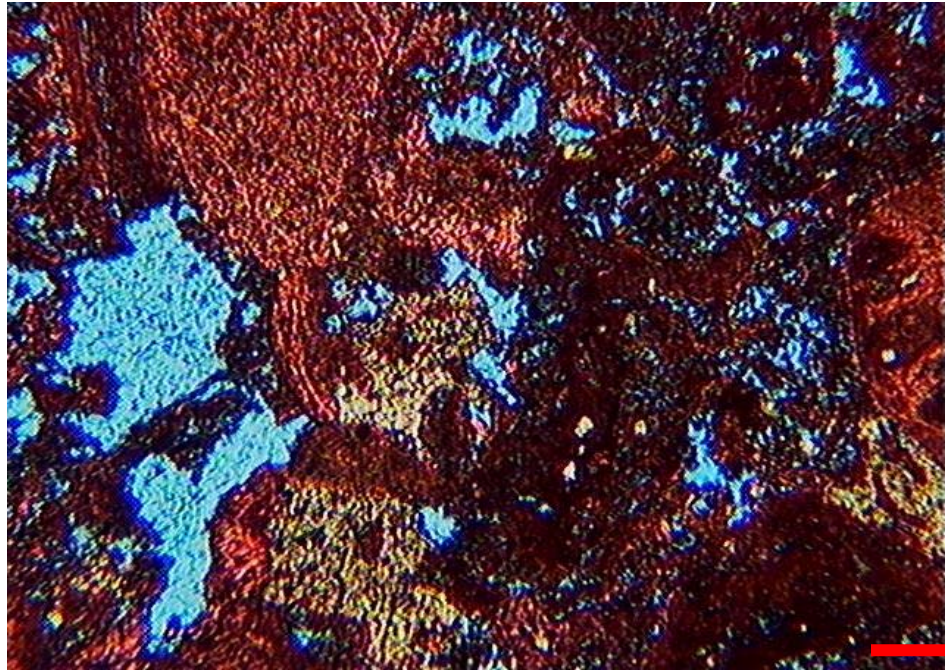


Figure 45. Photomicrograph of non-touching vugs. Sample is from Lott 19 #8 well, 4987.5' and is seen on Figure 44 as the outlier data point. Scale bar is 100 microns.

CONCLUSIONS

1. Happy Spraberry field produces from heterogeneous, shallow-shelf carbonates where lateral and vertical variations in porosity and permeability are common.
2. Porosity is predominantly a diagenetic overprint on depositional texture (grain-moldic in oolitic grainstones).
3. Analyses of carbonate pores utilizing petrographic image analysis methods is a relatively new procedure for gathering data on pore characteristics and is much faster than standard petrographic methods.
4. Image analysis data were interpreted to identify 4 distinctive pore facies which, in turn, are predictors of rock type, petrophysical properties, and production characteristics.
5. Image analysis is a reasonable substitute for determining porosity values obtained by alternate methods of core analyses, wireline log analyses, and standard petrographic methods.

6. The highest quality reservoir rocks occur in oolitic grainstones and packstones and, furthermore, the presence of moldic pores (oomoldic or skelmoldic) larger than 10,000 microns² combined with large, solution enhanced intergranular pores provide for optimum porosity and permeability.
7. Pore size obtained from petrographic image analysis is a useful predictor of median pore throat aperture, which would otherwise only be available by performing expensive Mercury injection capillary pressure tests.
8. Pitfalls of petrographic image analysis include choosing a magnification which gives appropriate and accurate images of porosity, quality control on preparation of thin-section samples, and consistent sampling of thin sections.
9. Petrographic image analysis has applicability in the geosciences (grain size, paleontology, fractures...) here it was implemented as a reservoir characterization tool within the carbonate interval at Happy Spraberry field.

REFERENCES CITED

- Ahr, W.M. and B.S. Hammel, 1999, Identification and mapping of flow units in carbonate reservoirs; An example from the Happy Spraberry (Permian) Field, Garza County, Texas USA: *Energy Exploration & Exploitation*, v. 17, p.311-334.
- Anselmetti, F. S., S. Luthi, and G.P. Eberli, 1998, Quantitative characterization of carbonate pore systems by digital image analysis: *AAPG Bulletin*, v. 82, p. 1815-1836.
- Archie, G.E., 1952, Classification of carbonate reservoir rocks and petrophysical considerations: *AAPG Bulletin*, v. 36, p. 278-298.
- Asquith, G., 1997, Basic well log analysis for geologists, *in* G. Asquith and C. Gibson, eds., *AAPG Methods in Exploration 3*, p. 66-90.
- Atchley, S. C., M. G. Kozar, and L. A. Yose, 1999, A predictive model for reservoir distribution in the Permian (Leonardian) Clear Fork and Glorieta formations, Robertson Field area, West Texas: *AAPG Bulletin*, v. 83, p. 1031-1056.
- Choquette, P.W., and L.C. Pray, 1970, Geologic nomenclature and classification of porosity in sedimentary carbonates: *AAPG Bulletin*, v. 2, p. 207-250.
- Dorobek, S. L., J.F. Read, and J.M. Niemann, 1987, Image analysis of cathodoluminescent-zoned calcite cements: *Journal of Sedimentary Petrology*, v. 57, p. 766-770.
- Dunham, R. J., 1962, Classification of carbonate rocks according to depositional texture, *in* W. E. Ham, ed., *Classification of carbonate rocks-a symposium: AAPG Memoir 1*, p. 108-121.

- Ehrlich, R., S.J. Crabtree, K.O. Horkowitz, and J.P. Horkowitz, 1991a, Petrography and reservoir petrophysics I: Objective classification of reservoir porosity: AAPG Bulletin, v. 75, p. 1547-1562.
- Ehrlich, R., E.L. Etris, D. Brumfield, L.P. Yuan, and S.J. Crabtree, 1991b, Petrography and reservoir petrophysics III: Physical models for permeability and formation factor: AAPG Bulletin, v. 75, p. 1579-1592.
- Ehrlich, R., and J. P. Horkowitz, 1987, Estimation of petrophysics from thin section; petrographic image analysis, *in* AAPG 1987 Southwest Section meeting; abstracts: AAPG Bulletin, Tulsa, OK, American Association of Petroleum Geologists, p. 238.
- Ehrlich, R., S. K. Kennedy, S. J. Crabtree, and R. L. Cannon, 1984, Petrographic image analysis; I, Analysis of reservoir pore complexes: Journal of Sedimentary Petrology, v. 54, p. 1365-1378.
- Hammel, B. S., 1996, High resolution reservoir characterization of the Permian (upper Leonardian) Spraberry Formation, Happy Spraberry Field, Garza County, Texas: Unpublished Master's Thesis, Texas A&M University, 1996, 157 pp.
- Handford, C. R., 1981, Sedimentology and genetic stratigraphy of Dean and Spraberry formations (Permian), Midland Basin, Texas: AAPG Bulletin, v. 65, p. 1602-1616.
- Jeary, G. L., 1978, Leonardian strata in the northern Midland Basin of West Texas, *in* R. L. Gilbertson, ed., Energy quest for the Southwest.: Publication - West Texas Geological Society, Midland, TX, West Texas Geological Society, p. 30-47.

- Lucia, F.J., 1983, Petrophysical parameters estimated from visual description of carbonate rocks: a field classification of carbonate pore space: *Journal of Petroleum Technology*, v. 35, p. 626-637.
- Mazzullo, S. J., and W. E. Hipke, 1991, Evolution of a mixed carbonate-siliciclastic platform; Lower Permian, northern Midland Basin, Texas, *in* AAPG Southwest Section meeting; abstracts : *AAPG Bulletin*, Tulsa, OK, American Association of Petroleum Geologists, p. 201.
- Mazzullo, S. J. and A. M. Reid, 1989, Lower Permian platform and basin depositional systems, northern Midland Basin, TX, *in* P.D. Crevello, J.L. Wilson, J.F. Sarg, J.F. Read, eds., *Controls on carbonate platform and basin development: SEPM Special Publication No. 44*, p. 305-320.
- McCreesh, C. A., R. Ehrlich, and S.J. Crabtree, 1991, Petrography and reservoir petrophysics II: Relating thin section porosity to capillary pressure, the association between pore types and throat size: *AAPG Bulletin*, v. 75, p. 1563-1578.
- Montgomery, S. L., and W. H. Dixon, 1998, New depositional model improves outlook for Clear Fork infill drilling: *Oil and Gas Journal*, v. 96, p. 94-98.
- Mowers, T. T., and D. A. Budd, 1996, Quantification of porosity and permeability reduction due to calcite cementation using computer-assisted petrographic image analysis techniques: *AAPG Bulletin*, v. 80, p. 309-322.
- Parham, K.D. and P.G. Sutterlin, 1993, Oolite shoals of the Mississippian St. Louis formation, Gray County, Kansas: A guide for oil and gas exploration: *in* *Mississippian Oolites and Modern Analogs*, Special Publication 35, p. 185-197.

- Ross, C.A., 1986, Paleozoic evolution of southern margin of Permian basin: Geological Society of America Bulletin, v. 97, p. 536-554.
- Roy, E., 1998, High resolution mapping of flow units for enhanced recovery program planning, Happy Spraberry Lime Field, Garza County, Texas: Unpublished Master's Thesis, Texas A&M University, 1998, 106 pp.
- Sano, H., K. Horibo, and Y. Kumamoto, 1990, Tubiphytes-Archaeolithoporella-Girvanella reefal facies in Permian buildup, Mino terrane, central Japan: Sedimentary Geology, v. 68, p. 293-306.
- Ward, R. F., C.G Kendall, and P.M Harris, 1986, Upper Permian (Guadalupian) facies and their association with hydrocarbons-Permian basin, West Texas and New Mexico: AAPG Bulletin, v. 70, p. 239-262.
- Wardlaw, N. C., 1976, Pore geometry of carbonate rocks as revealed by pore casts and capillary pressure: AAPG Bulletin, v. 60, p. 245-257.
- Wardlaw, N.C., 1979, Pore systems in carbonate rocks and their influence on hydrocarbon recovery efficiency: April 1979 short course on carbonate porosity, Department of Geology, University of Calgary, Calgary, Canada, p. E1-E24.
- Yang, K. M., and S.L. Dorobek, 1994, The Permian Basin of west Texas and New Mexico: Tectonic history of a "composite" foreland basin and its effect on stratigraphic development, *in* S.L. Dorobek and G. M. Ross, eds., Stratigraphic evolution of foreland basins, SEPM Special Publication no. 52, p. 147-172.

APPENDIX A

Core Description
 Bennett Petroleum
 Lott 19 #2
 Happy Spraberry Field
 Garza County, Texas
 Core Interval 4914.0'-4944.0'

Depth (ft.)	Thickness (ft.)	Description
4914.0	2.0	Limestone. Light gray to dark brown, very fine grained packstone, well sorted, mostly ooids/peloids and mollusk fragments, massive, grain moldic porosity, differential oil staining
4916.0	4.0	Core removed for special core analysis.
4920.0	2.0	Siltstone and shale. Dark gray, very fine grained quartz silt and clay. Fossils rare. Parallel to rippled laminations.
4922.0	3.0	Limestone. Brown to medium gray, moderately sorted grainstone. Ooids, peloids, and lithoclasts. Brachiopods, crinoids, and mollusks, massive, differential oil staining.
4925.0	1.0	Siltstone. Light to medium gray, very fine grained quartz. Calcite cementation, rippled to planar laminations, microfaults.
4926.0	9.0	Limestone. Medium gray to dark brown, well sorted, fine grained grainstone. Rare fossils, massive, imbricated lithoclasts, grain moldic and vuggy porosity.
4935.0	1.0	Siltstone. Light to medium gray, fine grained quartz. No fossils. Rippled laminations, microfaults.
4936.0	8.0	Limestone. Dark brown to medium gray, fine grained grainstone. Rare fossils, massive with isolated, planar ripples. Differential oil staining, vuggy and grain moldic porosity.

Core Description
 Bennett Petroleum
 Lott 19 #2 (cont.)
 Happy Spraberry Field
 Garza County, Texas
 Core Interval 4944.0'-4991.0'

Depth (ft.)	Thickness (ft.)	Description
4944.0	5.0	Core removed for special core analysis.
4949.0	1.0	Limestone. Light gray, moderately sorted packstone. Composed of mostly ooids, lithoclasts, and skeletal fragments. Mollusks, crinoids, brachiopods, and ostracods common.
4950.0	5.0	Limestone. Medium gray to dark brown, well sorted, fine grained grainstone. Massive, differential oil staining, grain moldic porosity.
4955.0	1.0	Sandstone. Light gray, moderately sorted very fine grained sandstone with skeletal packstone stringers. Mollusk, crinoids common, planar, wavy laminations.
4956.0	8.0	Siltstone. Light gray to medium gray, well sorted quartz grains, fossils very rare. Discontinuous wavy laminations, microfaulted with contorted bedding.
4964.0	16.0	Siltstone. Medium gray to dark gray, moderately sorted quartz grains. Fossils rare, Continuous wavy to planar laminations, microfaulted.
4980.0	11.0	Mudstone. Dark gray to black, well sorted clay particles. Fossils rare, continuous wavy laminations.
4991.0	-----	END OF CORE.

Core Description
 Bennett Petroleum
 Lott 19 #4
 Happy Spraberry Field
 Garza County, Texas
 Core Interval 4910.0'-4948.0'

Depth (ft.)	Thickness (ft.)	Description
4910.0	2.0	Limestone. Medium gray to dark brown, fine grained, moderately sorted packstone. Rare fossils, lithoclasts, and ooids, massive. Grain moldic porosity and differential oil staining.
4912.0	2.0	Limestone. Light gray, fine grained, well sorted grainstone. Composed of ooids, skeletal fragments, massive, with grain moldic and vuggy porosity.
4914.0	3.0	Limestone. Medium gray, very fine grained packstone, composed of ooids and peloids. Massive with undifferentiated skeletal fragments.
4917.0	1.0	Siltstone. Tan to dark gray, very fine grained quartz grains. Rare fossils, parallel to planar laminations, microfaulted.
4918.0	24.0	Limestone. Medium gray to light gray, fine grained grainstone. Moderately sorted, rare fossils, composed primarily of ooids and peloids. Anhydrite pore-filling cement. Well-developed grain moldic porosity.
4942.0	2.0	Limestone. Medium gray, fine grained moderately sorted silty packstone. Rare fossils, stylolites, microfaults, parallel, wavy, continuous laminations.
4944.0	4.0	Light gray to dark brown, very fine grained grainstone, composed mostly of ooids and peloids, burrowing.

Core Description
 Bennett Petroleum
 Lott 19 #4 (cont.)
 Happy Spraberry Field
 Garza County, Texas
 Core Interval 4948.0' - 4970.0'

Depth (ft.)	Thickness (ft.)	Description
4948.0	1.0	Limestone. Medium gray, moderately sorted fine grained packstone. Composed of skeletal fragments and ooids, wavy, discontinuous laminations.
4949.0	2.0	Limestone. Medium gray to dark brown, fine grained grainstone, composed of ooids, peloids and rare skeletal fragments. Massive, differential oil staining, grain moldic and vuggy porosity.
4951.0	5.0	Core removed for special core analysis.
4956.0	5.0	Limestone. Medium gray to dark brown, fine grained grainstone, composed of ooids, peloids and rare skeletal fragments. Massive, differential oil staining, grain moldic and vuggy porosity.
4961.0	3.5	Limestone. Light gray to medium gray, coarse grained, poorly sorted skeletal rudstone. Composed of oolitic grainstone lithoclasts and skeletal fragments, mostly of crinoid and bryozoan debris. Massive, brecciated texture.
4964.5	.5	Limestone. Medium gray to light tan, in situ biotic growth bindstone, mainly of bryozoans, ostracods, and crinoids. Growth fabric of sediment trapping and binding organisms.
4965.0	5.0	Limestone. Medium gray to medium tan, coarse grained skeletal, lithoclastic rudstone. Crinoids, mollusk, and oolitic grainstone lithoclasts.

Core Description
 Bennett Petroleum
 Lott 19 #4 (cont.)
 Happy Spraberry Field
 Garza County, Texas
 Core Interval 4970.0'-4981.0'

Depth (ft.)	Thickness (ft.)	Description
4970.0	1.0	Limestone. Light gray to light tan, in situ growth fabric. Fenestrate bryozoans, encrusting algae, Tubiphytes, and crinoids common.
4971.0	1.0	Limestone. Medium gray to dark tan, very coarse grained, poorly sorted, lithoclastic, floatstone. Oolitic grainstone lithoclasts and skeletal fragments, mainly of crinoids and mollusks.
4972.0	5.0	Siltstone. Light tan to light gray, very fine grained quartz grains with calcite cement. Parallel to wavy laminations, microfaulted.
4977.0	2.0	Limestone. Light gray, very coarse grained lithoclastic rudstone. Lithoclasts are composed primarily of oolitic grainstone and skeletal fragments.
4979.0	1.5	Limestone. Medium gray to dark gray, poorly sorted lime floatstone. Shaly matrix with isolated skeletal and lithoclasts fragments. Crinoid and bryozoan fragments common, with rare ooids and peloids.
4980.5	.5	Limestone. Medium gray to medium tan, in situ bindstone biotic growth. Bryozoans, brachiopods, and crinoids common. Anhydrite pore-filling cement.

Core Description
 Bennett Petroleum
 Lott 19 #4 (cont.)
 Happy Spraberry Field
 Garza County, Texas
 Core Interval 4981.0'-4994.0'

Depth (ft.)	Thickness (ft.)	Description
4981.0	4.0	Limestone. Medium gray to light tan, poorly sorted, floatstone. Silty matrix with light tan skeletal rudstone breccia. Composed of mostly crinoid, bryozoan, and mollusk fragments.
4985.0	1.0	Limestone. Dark gray to light gray, coarse grained rudstone. Fossils common with lithoclasts. Massive structure with brecciated texture.
4986.0	1.0	Limestone, dark gray to black, poorly sorted lime floatstone. Silty shale matrix with rudstone and bindstone lithoclasts, fossil fragments of crinoids and bryozoans common.
4987.0	2.0	Limestone. Dark gray to black, very fine grained mudstone. No fossils, wavy continuous to discontinuous laminations, microfaults, contorted bedding.
4989.0	2.0	Limestone. Dark gray, poorly sorted lime floatstone. Shaly matrix with rudstone and bindstone lithoclasts, fossil fragments of crinoids, bryozoans, and Tubiphytes.
4991.0	3.0	Siltstone. Dark gray to medium gray, very fine grained quartz. Isolated skeletal fragments, including ostracods, brachiopods, and crinoids. Continuous, wavy laminations.
4994.0	-----	END OF CORE.

Core Description
 Bennett Petroleum
 Lott 19 #5
 Happy Spraberry Field
 Garza County, Texas
 Core Interval 4926.0'-4960.0'

Depth (ft.)	Thickness (ft.)	Description
4926.0	5.0	Limestone. Light gray to medium gray, fine grained moderately sorted, silty, oolitic skeletal grainstone. Mudstone lithoclasts, skeletal fragments, parallel, continuous laminations, microfaults. Spotty oil staining rare.
4931.0	6.0	Siltstone. Medium gray to black, very fine grained siltstone. Calcite cement, isolated skeletal packstone stringers, continuous, wavy laminations, shaly discontinuous laminations, microfaults.
4937.0	5.0	Limestone. Light tan to dark brown. Very fine grained oolitic skeletal grainstone. Skeletal fragments including crinoids, ostracods, and bryozoans. Massive, imbricated mudpebble lithoclasts, grain moldic porosity, differential oil staining.
4942.0	5.0	Limestone. Light tan to light gray, fine grained oolitic grainstone. Calcite cement banding in tight spots. Continuous, wavy, non-parallel laminations, grain moldic porosity, spotty oil staining.
4947.0	1.0	Siltstone. Dark gray to black, very fine grained siltstone. Rare fossil fragments, calcite cement, continuous, wavy, parallel laminations.
4948.0	12.0	Limestone. Medium gray to light gray oolitic skeletal, fine grained grainstone. Mudstone lithoclasts, massive with isolated wavy, shaly, microfaulted laminations.

Core Description
 Bennett Petroleum
 Lott 19 #5 (cont.)
 Happy Spraberry Field
 Garza County, Texas
 Core Interval 4960.0'-5025.0'

Depth (ft.)	Thickness (ft.)	Description
4960.0	5.0	Core removed for special core analysis.
4965.0	2.0	Siltstone. Dark gray to medium gray, very fine grained siltstone with interbedded skeletal packstone stringers. Wavy, continuous, parallel laminations with microfaults.
4967.0	5.0	Limestone. Light tan to medium brown, fine grained, well sorted, oolitic and skeletal grainstone. Common ostracods, crinoids, and mollusks. Spotty oil staining with well developed grain moldic porosity.
4972.0	1.0	Limestone. Medium tan, poorly sorted, oolitic grainstone. Lithoclast present include reefy fragments as well as whole fossils. Grain moldic porosity.
4973.0	4.0	Siltstone. Light gray to medium gray, very fine grained quartz. Fossil fragments, calcite cement common, discontinuous, non-parallel laminations.
4977.0	7.0	Mudstone. Dark gray to black mudstone. Wavy, discontinuous laminations, microfaults, and contorted bedding.
4984.0	3.0	Siltstone. Medium gray very fine grained quartz. Fossil fragments rare, discontinuous, non-parallel laminations, microfaults.
4987.0	38.0	Lost core.

Core Description
Bennett Petroleum
Lott 19 #5 (cont.)
Happy Spraberry Field
Garza County, Texas
Core Interval 5025.0'

Depth (ft.)	Thickness (ft.)	Description
5025.0	-----	END OF CORE.

Core Description
 Bennett Petroleum
 Lott 19 #7
 Happy Spraberry Field
 Garza County, Texas
 Core Interval 4936.0'-4969.0'

Depth (ft.)	Thickness (ft.)	Description
4936.0	7.0	Siltstone. Light gray to light tan, very fine grained siltstone with interbedded skeletal packstone stringers. Skeletal fragments consist of mollusks, crinoids, and bryozoans. Continuous, parallel laminations with microfaults.
4943.0	3.0	Limestone. Medium gray, moderately sorted, silty skeletal packstone. Rare lithoclasts, crinoid fragments. Continuous, parallel, wavy laminations with microfaults.
4946.0	1.0	Siltstone. Medium gray to dark gray, very fine grained siltstone. Fossils rare, wavy, continuous, parallel laminations with microfaults.
4947.0	3.0	Limestone. Light gray to light tan, fine grained, well sorted, grainstone. Composed primarily of ooids and peloids. Skeletal fragments common, rare anhydrite cement, massive. Differential oil staining with grain moldic porosity.
4950.0	19.0	Limestone. Light gray to dark tan, poorly sorted skeletal rudstone/packstone. Anhydrite cement common, fossils include ostracods, bryozoans, mollusks, and crinoids, massive, non-bedded. Vuggy and grain moldic porosity, differential oil staining.

Core Description
 Bennett Petroleum
 Lott 19 #7 (cont.)
 Happy Spraberry Field
 Garza County, Texas
 Core Interval 4969.0'-5010.0'

Depth (ft.)	Thickness (ft.)	Description
4969.0	1.0	Limstone. Light gray to medium gray, poorly sorted, silty, lime wackestone. Wavy, discontinuous, non-parallel laminations, stylolites, and lithoclasts.
4970.0	18.0	Limestone. Medium gray to dark tan, poorly sorted, skeletal rudstone/packstone. Fossils include mollusks, bryozoans and crinoids. Massive, non-bedded, brecciated texture. Vuggy and grain-moldic porosity, differential oil staining.
4988.0	8.0	Siltstone. Light gray to light tan, well sorted very fine grained quartz grains. Rare, isolated skeletal fragments. Discontinuous, non-parallel, wavy laminations with microfaults.
4996.0	2.0	Limestone. Light gray, poorly sorted, silty skeletal lithoclastic rudstone. Brecciated texture, massive.
4998.0	6.0	Siltstone. Dark gray to medium gray, well sorted, fine grained quartz grains. Discontinuous, wavy, non-parallel laminations with microfaults.
5004.0	6.0	Siltstone. Moderately sorted, fine grained quartz grains. Minor lithoclasts with skeletal fragments composed primarily of crinoids and mollusks. Anhydrite cement with no visible porosity.

Core Description
 Bennett Petroleum
 Lott 19 #7 (cont.)
 Happy Spraberry Field
 Garza County, Texas
 Core Interval 5010.0'-5057.0'

Depth (ft.)	Thickness (ft.)	Description
5010.0	32.0	Siltstone. Light gray to medium gray, well sorted, very fine grained quartz. Continuous, wavy, parallel laminations. No fossils.
5042.0	9.0	Mudstone. Dark gray to black, moderately sorted, very fine grained silty mudstone. Isolated continuous, parallel laminations with microfaults.
5051.0	6.0	Siltstone. Medium gray, moderately sorted, fine grained quartz. Fossil fragments of crinoids and bryozoans common. Continuous, parallel, wavy laminations.
5057.0	-----	END OF CORE.

Core Description
 Bennett Petroleum
 Lott 19 #11
 Happy Spraberry Field
 Garza County, Texas
 Core Interval 4873.0'-4927.0'

Depth (ft.)	Thickness (ft.)	Description
4873.0	8.0	Limestone. Medium tan to light gray, moderately sorted, fine grained oolitic grainstone. Anhydrite replacement cement, fossils rare. Isolated continuous, wavy, parallel laminations, with minor microfaults. Grain moldic porosity and differential oil staining.
4881.0	2.0	Limestone. Light gray to light tan, poorly sorted, oolitic grainstone with mud pebble lithoclasts. Anhydrite cement, grain moldic porosity.
4883.0	1.0	Limestone. Light tan, well sorted, fine grained oolitic grainstone. Fossils rare, grain moldic porosity, differential oil staining.
4884.0	2.0	Lost core.
4886.0	38.0	Limestone. Light gray to medium tan, well sorted, fine grained oolitic skeletal grainstone. Anhydrite replacement cement, abundant fossil fragments, including mollusks, ostracods, and crinoids. Massive, non-bedded, grain moldic porosity of ooids and skeletal fragments, differential oil staining.
4924.0	3.0	Limestone. Light gray to medium gray, moderately sorted, fine grained, silty, oolitic skeletal packstone. Anhydrite cement, with isolated continuous, wavy, parallel laminations. Skeletal grainstone stringers with grain moldic porosity.

Core Description
 Bennett Petroleum
 Lott 19 #11 (cont.)
 Happy Spraberry Field
 Garza County, Texas
 Core Interval 4927.0'-4986.0'

Depth (ft.)	Thickness (ft.)	Description
4927.0	14.0	Lost core.
4941.0	11.0	Limestone. Light gray to medium gray, poorly sorted, skeletal rudstone. Pervasive anhydrite cement, abundant skeletal fragments, including bryozoans, mollusks, crinoids, and ostracods. Massive with stylolites and differential oil staining.
4952.0	5.0	Limestone. Light gray to light tan, well sorted, fine grained skeletal packstone grainstone. Massive, fossils include mollusks, bryozoans, and crinoids. Vuggy porosity and differential oil staining.
4957.0	19.0	Limestone. Light gray to medium tan, poorly sorted, skeletal rudstone. Pervasive anhydrite cement, fossils include mollusks and bryozoans with some intervals as in situ bindstones. Vuggy porosity with differential oil staining.
4976.0	1.0	Siltstone. Medium gray, moderately sorted, very fine grained quartz with isolated fossil fragments. Isolated packstone stringer, contorted bedding and soft sediment deformation.
4977.0	9.0	Siltstone. Medium gray to dark gray, very fine grained quartz grains with interbedded mudstone. No fossils, wavy, continuous, parallel laminations with microfaults.
4986.0	-----	END OF CORE.

APPENDIX B

Lott 19 #4 Petrographic Data

Depth (ft)	Porosity	Grains	Cement	Matrix	Quartz
4911.5	18	18	42	21	1
4919.3	21	12	58	9	0
4923.8	27	28	30	15	0
4926.9	32	10	47	9	2
4930.1	24	19	38	17	2
4933.1	18	24	47	11	0
4937.5	30	19	41	6	4
4940.8	32	27	33	4	4
4944.9	19	13	30	27	11
4949.5	7	6	8	38	41
4957.5	24	27	28	18	3
4960.6	20	43	25	9	3
4961.7	22	38	19	16	5
4963.5	10	39	6	25	20
4964.8	9	40	32	16	3
4970.6	20	28	21	27	4
4971.4	20	28	18	22	12
4972.9	18	37	8	27	10
4975.4	18	2	6	9	65
4980.7	11	36	24	22	7
4983.7	5	49	10	20	16

Lott 19 #7 Petrographic Data

Depth (ft)	Porosity	Grains	Cement	Matrix	Quartz
4936.4	12.0	0	8	15	65
4941.7	2.0	17	16	22	43
4945.9	4.0	20	47	10	19
4947.5	8.0	19	19	52	2
4949.3	26.0	9	58	6	1
4950.8	12.0	32	38	12	6
4954.7	17.0	12	30	34	7
4958.4	13.0	5	41	41	0
4963.2	18.0	7	19	56	0
4967.2	18.0	41	32	7	2
4970.2	11.0	36	23	26	4
4972.6	20.0	21	43	16	0
4975.4	17.0	6	44	33	0
4978.9	21.0	37	35	6	1
4981.2	28.0	24	45	3	0
4985.7	22.0	38	14	26	0
4988.1	17.0	11	56	16	0
4991.6	20.0	2	7	4	67
4996.6	21.0	11	7	56	5
5004.2	8.0	16	30	9	37
5006.5	8.0	25	28	22	17

VITA

NAME: John Morgan Layman II

PERMANENT ADDRESS: John M. Layman
2732 Ferguson Drive
Harrisonburg, VA 22801

EDUCATION: Texas A&M University
College Station, TX
M.S. Geology, 2002

James Madison University
Harrisonburg, VA
B.S. Geology, 1995

PROFESSIONAL EXPERIENCE: TotalFinaElf Exploration and Production, Inc. ` Onshore Production and Development, 2001

PROFESSIONAL MEMBERSHIP: American Association of Petroleum Geologists
Geological Society of America
Houston Geological Society
Society for Sedimentary Geology (SEPM)

PUBLICATIONS:

LAYMAN II, JOHN M., and Wayne M. Ahr, Texas A&M University, Department of Geology & Geophysics, College Station, TX 77845; Pore Measurements by Petrographic Image Analysis: Implications for Rapid Identification and Ranking of Reservoir Flow Units, Happy Spraberry Field, Garza County, Texas: AAPG Bulletin, v. 85 (2001), no. 13 Supplement.

LAYMAN II, JOHN M., and Wayne M. Ahr, Texas A&M University, Department of Geology & Geophysics, College Station, TX 77845; Pore Measurements by Petrographic Image Analysis: Implications for Rapid Identification and Ranking of Reservoir Flow Units, Happy Spraberry Field, Garza County, Texas: AAPG Bulletin, v. 84, no. 11 (November 2000), p. 1867.

LAYMAN II, JOHN M., Texas A&M University, Department of Geology & Geophysics, College Station, TX 77845; Pore Measurements by Petrographic Image Analysis: Implications for Rapid Identification and Ranking of Reservoir Flow Units, Happy Spraberry Field, Garza County, Texas: GSA Abstracts with Programs, 2000, v. 32, no. 7, p. 178.